# 第 11 回
# 核燃焼プラズマ
# 統合コード研究会

# 11th Burning Plasma Simulation Initiative (BPSI) Meeting

日時：2013 年 12 月 19 日(木)－20 日(金)
場所：九州大学筑紫キャンパス
応用力学研究所 2 階大会議室

# 第11回核燃焼プラズマ統合コード研究会

# 11th Burning Plasma Simulation Initiative (BPSI) Meeting

(Ver.2)

日時：2013年12月19日(木)－20日(金)
場所：九州大学筑紫キャンパス　応用力学研究所2階大会議室

(20 min talk+5 min discuss or 15min talk+5min discuss)

12月19日(木)

9:00 – 9:10　はじめに　福山（京大）
(座長：福山)
9:10 – 9:35　講演1-1　若狭（RIST）
Heat Transport Simulation in LHD Plasmas Using the TASK3D code
9:35 – 10:00　講演1-2　本多（原子力機構）
JT-60Uにおける新古典トロイダル粘性の影響
10:00 – 10:25　講演1-3　宮戸（原子力機構）
トカマクプラズマにおけるＩＴＧ乱流とコールドパルスのシミュレーション

10:25 – 10:40　休憩

(座長：宮戸)
10:40 – 11:05　講演1-4　矢木（原子力機構）
Simulation study of nonlocal transport from edge to core in tokamak plasmas
11:05 – 11:30　講演1-5　村上（京大）
LHDにおける高Tiプラズマの統合シミュレーション
11:30 – 11:55　講演1-6　登田（核融合研）
ヘリカルプラズマでのイオン温度勾配乱流における熱拡散係数のモデリング
11:55 – 12:15　講演1-7　西岡（京大）
ヘリオトロンJのNBIプラズマにおける新古典イオンフローのモーメント法を用いた数値解析

12:15 – 13:15　昼休み

(座長：糟谷)
13:15 – 13:40　講演2-1　林（原子力機構）

ペレットによる ELM 制御の統合シミュレーション
13:40 – 14:05　講演 2-2　　　松山（原子力機構）
ペレット入射プラズモイドのドリフト機構のモデリングと実験との比較
14:05 – 14:30　講演 2-3　　　河野（九工大）
イオンサイクロトロン加熱におけるプラズマ波と RF シースの相互作用
14:30 – 14:50　講演 2-4　　　羽田（京大）
One-Dimensional Transport Analysis of ECRH Assisted Plasma Start-up in JT-60SA

14:50 – 15:05　休憩

(座長：林)
15:05 – 15:30　講演 2-5　　　滝塚（阪大）
Enhanced neo-classical resistivity due to the m/n = 1/1 MHD-mode deformation for tokamak hybrid scenario
15:30 – 15:55　講演 2-6　　　佐藤（核融合研）
陰的時間積分法を用いた MHD コードの開発
15:55 – 16:15　講演 2-7　　　糟谷（九大）
乱流計測シミュレータを用いた非拡散輸送過程の数値診断
16:15 – 16:35　講演 2-8　　　佐々木（九大）
直線型装置における乱流構造形成シミュレーション

16:35 – 16:50　休憩

(座長：滝塚)
16:50 – 17:10　講演 2-9　　　小菅（九大）
炉心－周辺結合領域における輸送モデリング
17:10 – 17:30　講演 2-10　　　大澤（九大）
タングステン空孔中の水素の特異構造とその材料への応用
17:30 – 17:50　講演 2-11　　　東（京大）
PARASOL コードによるトカマク周辺プラズマの粒子シミュレーション

17:50　散会

19:30 – 22:00　懇親会（十徳や筑紫口店にて）

12 月 20 日(金)

9:00 – 9:05 事務連絡
(座長：矢木)
9:05 – 9:30 講演 3-1 福山（京大）
ITER 統合モデリングの進展
9:30 – 9:55 講演 3-2 横山（核融合研）
統合輸送解析スイート TASK3D（a,p）開発と LHD 実験適用の進展
9:55 – 10:15 講演 3-3 金森（京大）
TASK/TX によるトカマク粒子輸送シミュレーション

10:15 – 10:20 休憩

(座長：横山)
10:30 – 10:55 講演 3-4 藤堂（核融合研）
DIII-D におけるアルフベン固有モードと高速イオン輸送のシミュレーション
10:55 – 11:20 講演 3-5 Lesur (九大)
Scheme-independent error in entropy conservation in turbulent kinetic simulations
11:20 – 11:45 講演 3-6 小関（原子力機構）
ITER 遠隔実験センター
11:45 – 12:00 まとめ 矢木

12:00 – 13:00 昼休み

13:00 – 17:00 核融合エネルギーフォーラムサブクラスター会合

17:00 散会

# Heat Transport Simulation in LHD Plasmas Using TASK3D code

A. Wakasa[1], A. Fukuyama[2], S. Murakami[2], N. Takeda[2], and, M. Yokoyama[3]
[1] Research Organization for Information Science and Technology, Tokai, 319-1106, Japan
[2] Department of Nuclear Engineering, Kyoto University, Sakyo-ku, Kyoto 606-8501, Japan
[3] National Institute for Fusion Science,322-6 Oroshi-cho, Toki 509-5292, Japan

## 1. Introduction

TASK3D[1] is an integrated transport simulation code for the helical plasmas. It is under development in collaboration with Kyoto University and NIFS and has been used to analyze a variety of LHD experiments so far. Using TASK3D, we have performed self-consistent calculation of the heat transport and heating profile for parameters in experiments (Experimental analysis) and predictive simulations assuming a variety of NBI heating conditions (Predictive analysis). In this study, in order to improve the accuracy of the turbulent transport model in TASK3D, we have made comparison and the validation of gyro-Bohm based transport models with LHD experimental results (14th, Sep. 2011).

## 2. Integrated simulation code, TASK3D

TASK3D has a modular structure and each module describes different physics phenomena. Figure 1 shows the flow diagrams of the 1D heat transport simulation using TASK3D. Here, TR is the 1D diffusive transport module, and solves particle transport equation, heat transport equation, and magnetic field equation. The neoclassical transport coefficients are calculated by the neoclassical transport database, DGN/LHD[2], and the radial electric field is calculated by the ER module, according to the ambipolar condition. The NBI power deposition profiles are calculated by FIT3D module in response to changes in the spatial profiles of temperature and density calculated by the TR module. Thus, we can perform self-consistent simulations of heat transport in NBI plasmas.

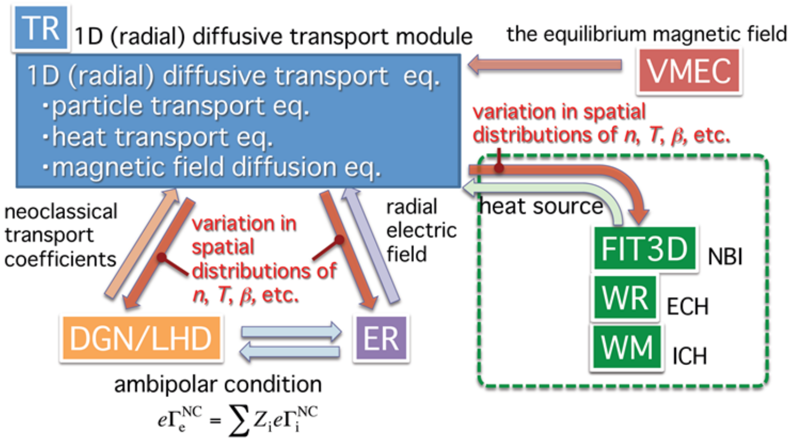

Fig. 1. The flow diagrams of 1D heat transport simulation using TASK3D

## 3. Predictive simulation with simple gyro-Bohm transport model

We assume that the thermal diffusion coefficients are given by the sum of a turbulent term $\chi^{\mathrm{TB}}$ and a neoclassical term $\chi^{\mathrm{NC}}$, $\chi = \chi^{\mathrm{TB}} + \chi^{\mathrm{NC}}$. We also assume $\chi_{\mathrm{e}}^{\mathrm{TB}}=\chi_{\mathrm{i}}^{\mathrm{TB}}$ and adopted a simple gyro-Bohm model, $\chi^{\mathrm{TB}}_{\mathrm{gyroBohm}} = \mathrm{C}_{\mathrm{gyroBohm}}\left(T/eB\right)\left(\rho_i/a\right)$, compatible with International Stellarator Scaling 95, ISS95[3]. Here, $\mathrm{C}_{\mathrm{gyroBohm}}$ is a constant factor, which is adjusted so that the simulation results well reproduce experimental observations. In this study, $\mathrm{C}_{\mathrm{gyroBohm}}$ is determined as $\mathrm{C}_{\mathrm{gyroBohm}} = 21.2$ to minimize the relative mean square error between experimental and simulation results of the reference shots. Using this value of $\mathrm{C}_{\mathrm{gyroBohm}}$, we have performed predictive heat transport simulation in LHD as shown Fig. 3(a). In order to validate the simulation results, the LHD experiments in the similar NBI heating condition and density profiles to the TASK3D simulation were performed as shown Fig. 3(b). $T_{\mathrm{e}}$ obtained by the predictive simulation is in good agreement with the experimental results, while $T_{\mathrm{i}}$ obtained by the predictive simulation is about 25% lower than the experimental results in the core region. In recent high $T_{\mathrm{i}}$ LHD experiments, the $T_{\mathrm{i}}$ profiles obtained by TASK3D with this simple gyro-Bohm model are also rather low in the plasma core region.

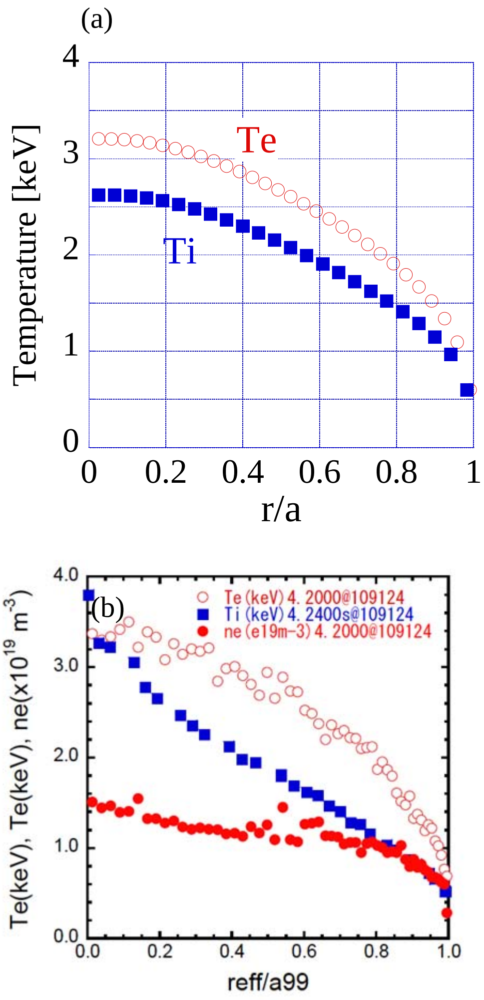

Fig. 3. (a) Rsults of Predictive simulation by TASK3D and (b) Experimental results under close condition with TASK3D simulation.

## 5. Summary

We have been developing the integrated simulation code TASK3D for non-axisymmetric plasmas. We have chosen the constant factor for a simple gyro-Bohm transport model, $\mathrm{C}_{\mathrm{gyro\text{-}Bohm}}$, using the recent LHD experimental results. Then, we have performed a predictive simulation and found that the predicated $T_{\mathrm{e}}$ is in good agreement with the experimental results, while the predicted $T_{\mathrm{i}}$ is less peaked compared with the experimentally observed profile.

**Acknowledgments** This work is supported in part by Grant-in-Aid for Scientific Research (S) (20226017) from JSPS and by the NIFS Collaboration Research program.

## References

[1] A. Wakasa et al., 23rd IAEA-FEC (2010).
[2] A. Wakasa et. al., Contrib. Plasma Phys. 50, No. 6-7, 582 585 (2010)
[3] U. Stroth et al., Nucl. Fusion 36, 1063 (1996).

# Effects of the neoclassical toroidal viscosity in JT-60U

M. Honda[1], S. Satake[2], Y. Suzuki[2], G. Matsunaga[1], K. Shinohara[1], M. Yoshida[1], H. Urano[1],
S. Ide[1] and N. Hayashi[1]

[1] Naka Fusion Institute, Japan Atomic Energy Agency
[2] National Institute for Fusion Science

The integrated code, the TOPICS suite, has recently gained the capability to self-consistently calculate the radial electric field $E_r$ and the evolution of poloidal and toroidal flows [1]. With the aid of the orbit-following Monte Carlo code OFMC, toroidal rotation driven by neutral beam injection (NBI) can be calculated in plasmas with the toroidal field (TF) ripple and thus the ripple effects on fast ions regarding a torque has already been investigated [1]. Recently the neoclassical toroidal viscosity (NTV) in tokamaks acting on thermal ions has attracted attention in that the NTV damps toroidal rotation towards a certain level of the rotation velocity, called the offset rotation. The NTV is a kind of the non-axisymmetric 3D effect in tokamaks due to the toroidally-asymmetric perturbed magnetic field that stems from not only the discrete TF coils but also their misalignment, MHD activities and the resonant magnetic perturbation. Given that in reality tokamaks are not axisymmetric, the NTV is ubiquitous and is therefore an indispensable piece of toroidal rotation predictions as a torque source especially localized in the edge region. In contrast, transport simulations with the NTV have seldom been performed. This is due partly to its complicated 3D nature and a lack of tools to numerically estimate it. A drift-kinetic $\delta f$ Monte Carlo code, FORTEC-3D, which has originally been developed for neoclassical transport analyses in heliotrons and stellarators, is able to compute the NTV [2,3], including effects of $E_r$ in tokamaks [4]. A numerical tool like FORTEC-3D has many advantages in that it does not essentially require any assumptions that are usually required in the course of the derivation of the analytic NTV formula and can adopt a real equilibrium geometry. The magnetic equilibrium including the plasma response by the perturbed magnetic field in vacuum can be computed by the 3D equilibrium code, VMEC [5].

The cooperative framework of TOPICS, VMEC and FORTEC-3D has been developed for the NTV analysis [6], as in detail shown in Fig.1. In this work, it is applied to JT-60U experimental analyses. Since JT-60U had somewhat larger TF ripple amplitude due partly to the circular TF coils, it can be speculated that the NTV potentially plays a non-negligible role in the formation of the toroidal rotation profile. We therefore compute the

NTV profile in JT-60U L-mode discharges w/ and w/o the ferritic steel tiles (FSTs) and study its impact on toroidal rotation by TOPICS simulations. Note that the boundary is set at $\rho$=0.95. As shown in Fig. 2(b), the NTV torque indeed lies in the edge region and its amplitude is comparable to or greater than the $j$×$B$ torque due to the NBI. It is found in Fig. 2(a) that including the NTV largely improves the reproducibility of predicted rotation profiles, a fact which indicates that the NTV is imperative as one of the major torque sources.

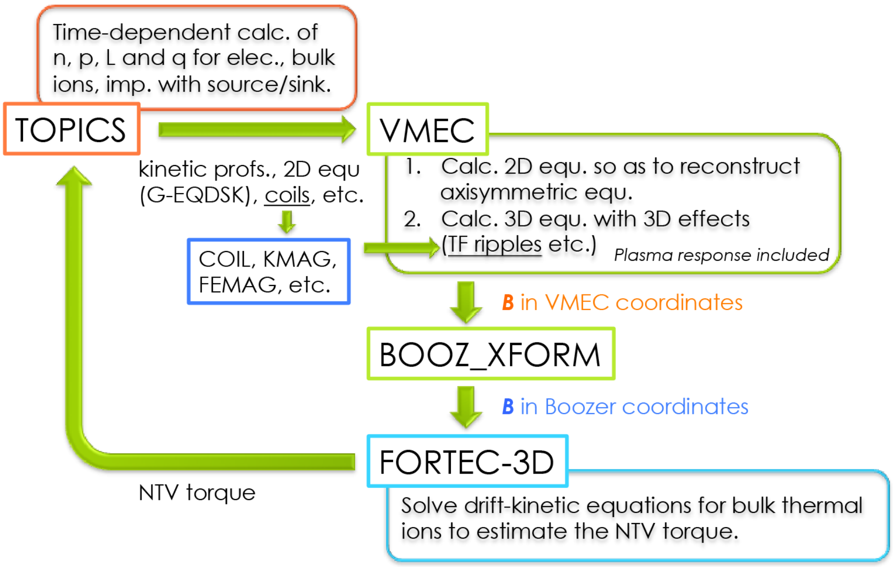

**Figure 1. The cooperative framework of TOPICS, VMEC and FORTEC-3D.**

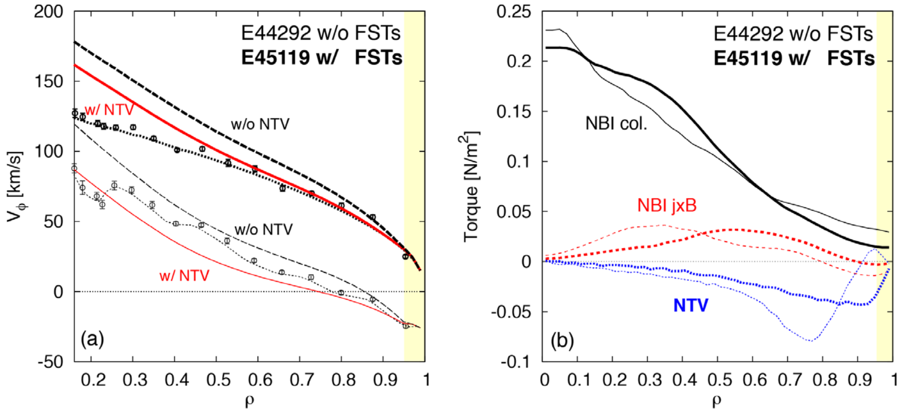

**Figure 2. (a) Carbon toroidal rotation profiles of the experimental observation (points with error bars and dotted lines), the predictions w/ and w/o the NTV (solid and dashed lines, respectively). (b) Torque profiles of the collisional and the $j$×$B$ transfers from the NBI and the NTV**

[1] M. Honda et al., *Nucl. Fusion* **53** (2013) 073050.

[2] S. Satake et al., *Plasma Phys. Control. Fusion* **53** (2011) 054018.

[3] S. Satake et al., *Phys. Rev. Lett.* **107** (2011) 055001.

[4] S. Satake et al., *Nucl. Fusion* **53** (2013) 113033.

[5] S. P. Hirshman and O. Betancourt, *J. Comput. Phys.* **96** (1991) 99.

[6] M. Honda et al., submitted to *Nucl. Fusion*.

# Simulation study of ion temperature gradient driven turbulence with cold pulse in a tokamak plasma

N. Miyato and M. Yagi

Japan Atomic Energy Agency, Rokkasho, Aomori

Nonlocal plasma responses which cannot be explained by the conventional local transport models are widely observed in toroidal plasmas [1]. For example, electron temperature in the core region rapidly increases by edge cooling before its effect reaches the core region diffusively. Recently, a nonlocal response of plasma to edge density sources is found in global fluid simulations which are based on the 4-field reduced magnetohydrodynamics (RMHD) model [2, 3]. In the nonlocal plasma response/transport found in the RMHD simulations both nonlinear and toroidal couplings between axisymmetric $n = 0$ Fourier modes are responsible, in particular $(m, n) = (\pm 1, 0)$ pressure fluctuations play a key role, where $m$ and $n$ are poloidal and toroidal mode numbers, respectively. Although the resistive ballooning modes are unstable at the edge, they do not play an important role in the nonlocal transport.

In the above RMHD simulations no turbulence exists in the core region where the nonlocal response appears. However, ion temperature gradient (ITG) driven turbulence is important for transport of tokamak core plasmas. The $(\pm 1, 0)$ pressure perturbations are the ingredient of oscillatory zonal flows (ZFs) or geodesic acoustic modes (GAMs) also [4]. The GAM frequency observed in global ITG simulations deviates from its local frequency and has some identical value over a certain radial distance [5]. Therefore, the nonlocal transport observed in the RMHD simulations may be affected by the ITG turbulence. We have modified the global Landau-fluid code used for the ITG turbulence simulations to include the toroidally elongated source used in the RMHD simulation [2]

$$S = S_{\mathrm{AMP}} \exp\left(-\frac{r^2 + r_s^2 - 2rr_s \cos\theta \cos\theta_s - 2rr_s \sin\theta \sin\theta_s}{2\Delta^2}\right) \tag{1}$$

where $S_{\mathrm{AMP}}$ is the source amplitude, $(r_s, \theta_s) = (0.8, 0)$ and $\Delta$=0.1 represent the source location in the poloidal plane and the half width of source, respectively. As a first step we perform electrostatic ITG simulations based on the 3-field Landau-fluid model in which the source is implemented as a sink or cold pulse in an ion temperature equation [5]. We use the parameters used in [5]: $\rho_i/a = 1/200$, $R/a = 4$, $\tau = T_e/T_i = 1$, $n_{eq} = 0.8 + 0.2\exp[-2(r/a)^2]$, $T_{eq} = 0.35 + 0.65[1 - (r/a)^2]^2$ and $q = 1.05 + 2(r/a)^2$. Fourier modes included in the following calculations are ones having resonant surfaces between $0.2 < r/a < 0.8$ with

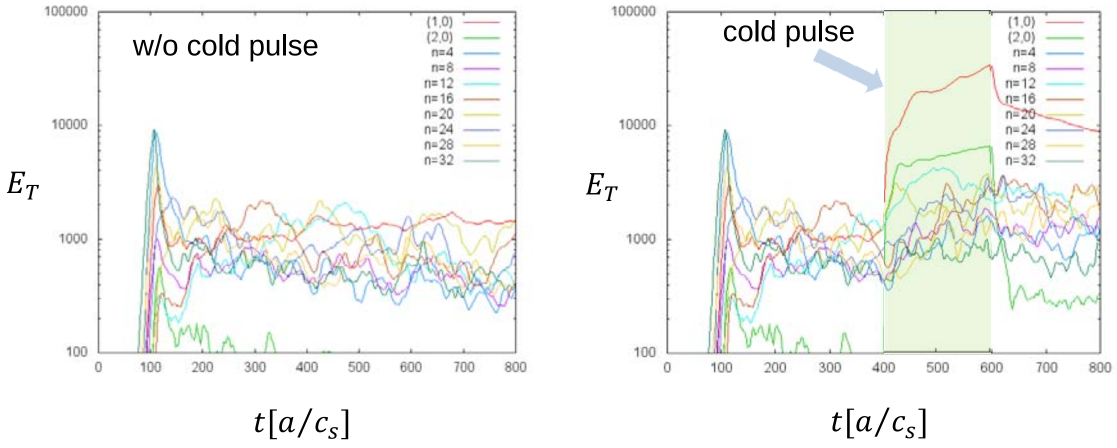

Fig.1: Temporal evolutions of ion temperature fluctuation energy.

$\Delta n = 4, n_{max} = 100$ and nonresonant ones with $n = 0$ and $|m| < 20$. Number of radial grids is 512. The code is well parallelized using Message Passing Interface (MPI) and OpenMP.

Figure 1 shows temporal evolutions of ion temperature fluctuation energy. As shown in the left panel, the $(1,0)$ component increases slowly and becomes larger than the turbulence fluctuations with $n \neq 0$, when no cold pulse is imposed. The $(1,0)$ component seems to be due to the GAMs driven by the turbulence. The cold pulse puts ion temperature fluctuation energy into $(m,0)$ components directly as shown in the right panel in which the cold pulse is imposed in the hatched region ($400 \leqq t \leqq 600$). The $n \neq 0$ turbulent fluctuations also increase during the cold pulse. This is due to profile steepening of ion temperature by the cold pulse. Excitation of the GAM oscillation of ZFs is observed around $r/a \sim 0.6 - 0.8$ from $t \sim 450$ a little after the start of the cold pulse. It is supposed that direct excitation of GAMs by the cold pulse is not so strong, rather they are excited by the turbulence strengthened.

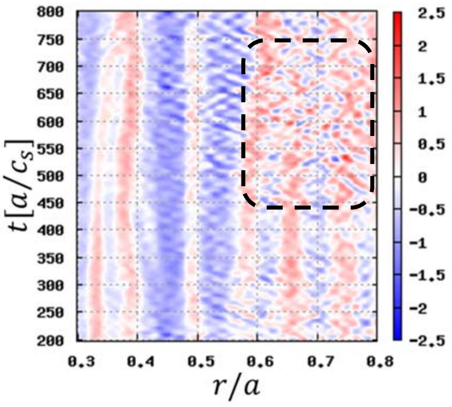

Fig.2: Zonal flow behavior

The computations were carried out on the HELIOS system at the IFERC-CSC, Rokkasho, Aomori, Japan.

[1] J. D. Callen and M. W. Kissick, Plasma Phys. Control. Fusion **39** (1997) B173.

[2] M. Yagi, et al., "Simulation study of nonlocal transport from edge to core in tokamak plasmas," to be published in Contrib. Plasma Phys.

[3] M. Yagi, et al., "Simulation study on nonlocal transport for peripheral density source," 23rd International Toki Conference (Toki, Japan, 21 Nov. 2013) P1-43.

[4] N. Miyato, Y. Kishimoto and J. Q. Li, Phys. Plasmas **11** (2004) 5557.

[5] N. Miyato, Y. Kishimoto and J. Q. Li, Plasma Phys. Control. Fusion **48**, A335 (2006).

# Simulation study of nonlocal transport from edge to core in tokamak plasmas

M. Yagi, M. Miyato, A. Matsuyama and T. Takizuka

Japan Atomic Energy Agency, Rokkasho, Aomori
Graduate School of Engineering, Osaka University, Suita, Osaka

The transient transport events are observed in the magnetic confinement devices[1,2]. The time scale of the transient transport is much faster than the diffusive time scale, which is difficult to explain based on the local transport model. Theoretically, the non-local transport model was proposed based on the one-dimensional integral heat flux model[3]. In this work, the non-local transport for peripheral density source is investigated by using 4-field reduced MHD model[4]. The spherical source is introduced in the density evolution equation

$$S = S_{AMP} \exp\left( -\frac{r^2 + r_s^2 - 2rr_s \cos\theta + \zeta^2 / \varepsilon^2}{2\Delta^2} \right) \tag{1}$$

where $S_{AMP} = 10^{-2}$, $r_s = 0.8$, $\Delta = 0.1$, $\varepsilon = 1/3$ are used. The spherical source is applied at t=960 after saturation of the resistive ballooning turbulence, which is excited in the peripheral region. Then, the source is switched off at t=1800. Figure 1 shows the time evolution of internal energy for each Fourier mode, which is defined by

$$E_{m,n} = \frac{1}{2}\int_0^1 r\, dr \left| p_{m,n}(r) \right|^2 \tag{2}$$

where *m* and *n* represent the poloidal and toroidal mode numbers. It is shown that the energy is directly transferred into (0,0) and (1,0) modes as well as finite n modes from the source at *T*=960. Figure 2 shows the time evolution of flux averaged total density profile at *T*=960, 1800, 2500, which is calculated by

$$p_{tot}(r) = p_{eq}(r) + p_{0,0}(r) \tag{3}$$

It is shown that the nonlocal transport appears after switching-on the source at *T*=1800. The $q$ -profile is also shown in Fig.2, where $q$ indicates the safety factor. Although the nonlocal transport appears in the vicinity of $q$ = 3/2 surface, it is not an exact location of $q$ = 3/2 surface.

The simulation result is summarized as follows: (1) When the spherical source is applied in the plasma edge, the energy is directly transferred into $p_{0,0}$ and $p_{1,0}$ modes as well as finite $n$ modes. (2) When the source is switched on, the dipole structure starts to deform and the spiral structure is formed by $p_{1,0}$ modes, which connects the core and the edge regions. (3) $p_{1,0}$ modes interact with $p_{0,0}$ via the three wave coupling and the toroidal coupling, which produces the nonlocal transport in the vicinity of $q = 3/2$ surface. We confirm this mechanism not only by simulations without the convective nonlinearity in $p_{0,0}$ evolution equation or without the toroidal coupling (in the cylinder limit). Comparing with the cylindrical source, it is found that the mechanism to produce the nonlocal transport is the same, however, it appears after switching-on the source for spherical source, on the other hand, it appears just after switching-off it for cylindrical source[5]. The nonlocal transport obtained in this simulation is driven by the macroscopic structure, which is consistent with experimental observation[6].

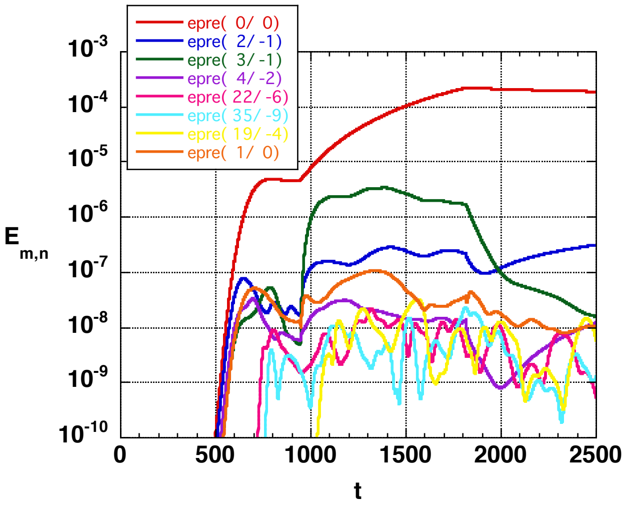

**Fig.1** *Time evolution of internal energy for each Fourier mode. The source is applied at t=960 and is switched off at t=1800.*

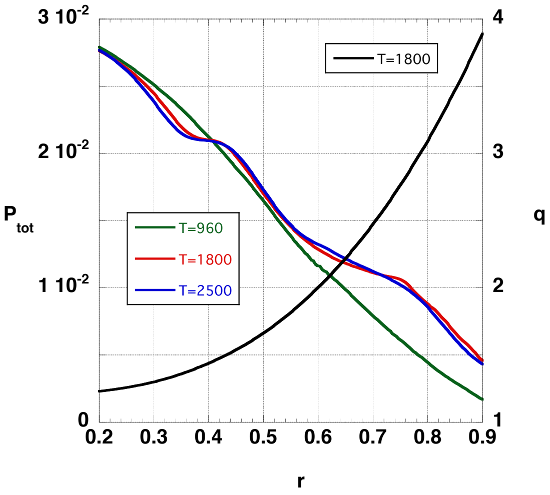

**Fig.2** *Time evolution of flux averaged total density profile at t=960(green), 1800(red), 2500(blue). q-profile at t=1800 is also plotted(black).*

This work is partially supported by Grant-in-Aid for Scientific Research (No. 23246163). The simulations are performed by using HELIOS super computer in IFERC-CSC, Aomori, Japan. The Collaborative Research Program of Research Institute for Applied Mechanics, Kyushu University is also acknowledged.

[1] U. Stroth, L Giannone, H-J Hartfuss, et al., Plasma Phys. Control. Fusion 38, 1087 (1996).
[2] N. Tamura, S. Inagaki, K. Ida, et al., Phys. Plasmas 12, 110705 (2005).
[3] T. Iwasaki, S.-I. Itoh, M. Yagi, et al., J. Phys. Soc. Jpn. 68, 478 (1999).
[4] M. Yagi, S. Yoshida, S.-I. Itoh, et al., Nucl. Fusion 45, 900 (2005).
[5] M. Yagi, A. Matsuyama, N. Miyato and T. Takizuka, 14th International Workshop on Plasma Edge Theory in Fusion Devices (Cracow Poland, 23-25 Sep. 2013).
[6] S. Inagaki, T. Tokuzawa, K. Itoh, et al., Phys. Rev. Lett. 107,115001 (2011).

# Integrated Heat Transport Simulation of High Ion Temperature Plasma of LHD

S. Murakami, H. Yamaguchi, A. Sakai, N. Nagaoka*, H. Takahashi*, H. Nakano*, M. Osakabe*, K. Ida*, M. Yoshinuma*, M. Yokoyama* A. Wakasa, A. Fukuyama and LHD Exp Group*

*Department of Nuclear Engineering, Kyoto Univ., Kyoto 606-8540, Japan*
**National Institute for Fusion Science, 322-6 Oroshi, Toki 509-5292, Japan*
*e-mail: murakami@nucleng.kyoto-u.ac.jp*

High ion temperature plasma with carbon pellet injection of LHD is investigated by the integrated heat transport simulation. NBI heating deposition of time evolving plasma is evaluated by GNET-TD and the heat transport of multi-ion species plasma (e, H, He, C) is studied by TASK3D. Achievement of high ion temperature plasma is attributed to the 1) increase of heating power per ion due to the temporal increase of Z-eff, 2) reduction of effective neoclassical transport with impurities, 3) reduction of turbulence transport. The reduction of turbulence transport is most significant contribution to achieve the high ion temperature and the reduction of the turbulent transport from the L-mode plasma (normal hydrogen plasma) is evaluated to be factor more than three by using integrated heat transport simulation code.

## Introduction

High ion temperature, $T_i$, experiments have been performed applying the tangential and perpendicular NBI heating systems in LHD[1]. The high $T_i$ plasma up to 7.3keV has been obtained during the decay phase of the density after rapid increase due to a carbon pellet injection. Simple heat transport analysis of these high $T_i$ plasma has been done but the rapid change of density effect on the NBI heat deposition and the multi-ion species effects on the heat transport is not treated accurately. In order to analyze the transport property of the time evolving plasma, we have to use NBI heat deposition analysis code including the effect of plasma time evolution. Also the plasma contains sufficient impurities due to the He gas puff and C pellet injection and the heat transport simulation should take care the multi-ion species.

In this paper we study the high $T_i$ plasma with C pellet injection of LHD applying the integrated simulation code GNET-TD and TASK3D. We perform time-dependent NBI heating simulation using GNET-TD code, which is a modified version of the 5D drift kinetic equation solver GNET[2]. Next we investigate the heat transport of high $T_i$ plasma assuming multi-ion species plasma (e, H, He, C) by the integrated transport code, TASK3D [3].

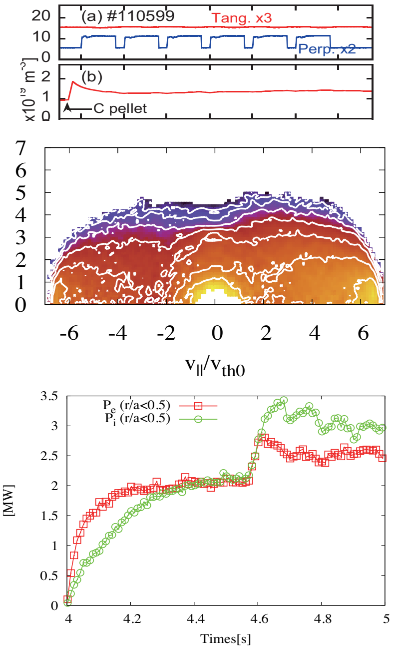

Figure 1: *(Top) Time history of NBI heating power and the density, (center) NBI beam ion distribution at t=4.7s, (bottom) Time history of NBI heat deposition.*

## NBI heating analysis of C-pellet injection plasma

In order to analyze the NBI heat deposition profile of time evolving plasma we have developed GNET-TD including the finite drift orbit and complex motion of trapped particles. We performed NBI heating simulation of high-$T_i$ discharge (# 110599) plasma, in which the plasma density changes in time. In the simulation time change of densities and temperature profiles are from the experimental measurements. For simplicity we assumed $Te = Ti$ because $V_{beam} >> V_i$ . There are five NBI injectors and one of them #4 is modulated in order to measure the ion temperature (Fig. 1-(top)).

We evaluate the beam ion distributions including time evolutions of density, temperature and beam power modulations. Before the C pellet injection beam ion distribution reaches a steady state slowing down distribution, and just after the pellet injection strong slowing down of energetic beam can be seen at the edge region. But we can not see clear change in the central region. After the density decay phase the beam distribution is recovered. Figure 1-(center) shows the beam ion distribution in velocity space after the pellet injection in the core region ($r/a < 0.5$). We can see the slowing down distribution of co and counter injected and perpendicular injected NBI beam ions. Figure 1-(bottom) shows the NBI heat deposition in the core region ($r/a < 0.5$). The heat deposition is jump up by the pellet injection and the start of the perpendicular #4 injector at $t = 4.575$s.

## Heat transport simulation of high-$T_i$ plasma

In order to perform the integrated heat transport simulation of high $T_i$ plasma we apply the improved TASK3D code assuming multi-ion species plasma (e, H, He, C). In TASK3D one dimensional diffusive transport is solved in the TR module. The heat source is loaded from the results of GNET-TD.We assume that the heat transport consists of the neoclassical and the turbulent ones. In TASK3D the neoclassical transport database, DGN/LHD, evaluates the neoclassical heat transport for all species and the radial electric field is determine by the am-bipolar condition of neoclassical electron and ion fluxes. For the turbulent transport we assume the gyro-Bohm model and the gyro-Bohm grad-$T_i$ model for the electron and ion heat conductions as $\chi_e^{TB} = C_e \left(\frac{T}{eB}\right)\left(\frac{\rho}{L}\right)$, $\chi_i^{TB} = C_i \left(\frac{T}{eB}\right)\left(\frac{\rho}{L}\right)\left(\frac{aT'}{T}\right)$, where $C_e$ and $C_i$ are the constant factors estimated by best fitting of the hydrogen L-mode (normal) shot profile data[3].

We perform the integrated heat transport simulation of high-$T_i$ discharge (# 110599) plasma using the density profiles from the experimental measurements. The electron temperature drops rapidly by the pellet injection and backed to the previous temperature. This shows similar behavior with the experimental one. The $T_i$ increases about 0.5keV just after the pellet injection until t=4.7s and gradually decreases. Also we found that the increment of $T_i$ after the pellet injection, $\Delta T_i$, increases more if we change the carbon density from the experimentally obtained values. This is due to the increase of heating power per ion by the temporal decrease of the ion number density and, also, due to the reduction of effective neoclassical transport with impurities by the C-pellet injection. However the increment of ion temperature is lower than that of experimental one ($\Delta T_i \simeq 3.5$keV). This indicates that the reduction of the turbulent transport is necessary to explain the observed high-$T_i$.

Next we introduce the confinement improvement factor, $\gamma_{TB}$, in the ion turbulent heat transport model as $\chi_i^{TB} = \frac{1}{\gamma_{TB}} C_i \left(\frac{T}{eB}\right)\left(\frac{\rho}{L}\right)\left(\frac{aT'}{T}\right)$. Also we introduce the carbon density factor, $f_C$, as $n_{Csim} = f_C \times n_{Cexp}$. Figure 2-(a) shows $\Delta T_i$, as a function of $\gamma_{TB}$ with different carbon densities. It is found that about 2keV of $\Delta T_i$ is obtained when we set $\gamma_{TB}$= 2.5 and that $\Delta T_i$ increases about 1keV when $f_C = 2.0$. Figure 2-(b) shows the time evolution of $\Delta T_i$ changing the carbon density with $\gamma_{TB}$= 2.5. We can see a rapid increase of $\Delta T_i$ and, then, the decrease gradually. This increase of $\Delta T_i$ is mainly due to the improvement of turbulent transport. It is also found that the increment of $\Delta T_i$ due to the increase of the carbon density.

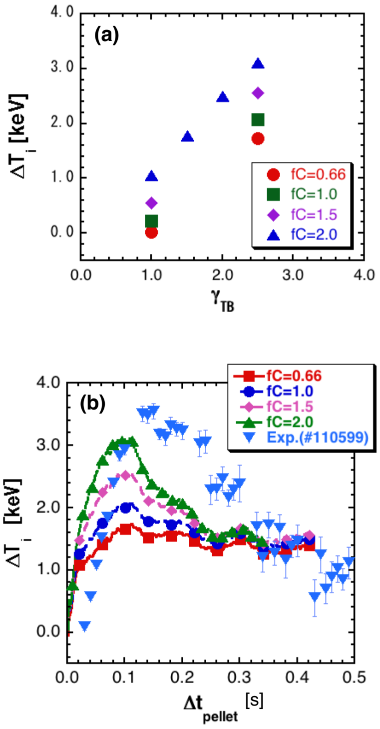

Figure 2: *(a) Increment of ion temperature after C-pellet injection, $\Delta T_i$, as a function of the improving factor, $\gamma_{TB}$ with different carbon densities. (b) Time history of $\Delta T_i$ changing the different carbon densities with $\gamma_{TB}$ =2.5.*

[1] H. Takahashi et al., Nucl. Fusion **53** (2013) 073034.

[2] S. Murakami et al., Nucl. Fusion **46** (2006) S425.

[3] A. Wakasa, et al., Proc. 39th EPS Conf. and 16th Int. Cong. Plasma Phys., 2012, **P2.028**.

# Modeling of Heat Diffusivity for Ion Temperature Gradient Turbulence in Helical Plasmas

S. Toda, M. Nunami, A. Ishizawa, T. -H. Watanabe, H. Sugama
*National Institute for Fusion Science, 322-6 Oroshi-cho, Toki 509-5292, Japan*

Turbulent transport is one of the most critical issues for plasma confinement in magnetic fusion devices. This is because the turbulent transport induces a large amount of the particle and heat loss in toroidal plasmas. Further study of the plasma turbulence and the transport is necessary for the improvement of the plasma performance. In the integrated transport analysis suite, TASK3D, which is the one-dimensional (the radial) transport code, the gyro-Bohm scaling on the heat turbulent diffusivities is used in LHD [1]. In the case of ITG turbulence, the form $\chi_i \sim \rho_{ti}^2 v_{ti} f(\gamma, \hat{s}, \tau_{ZF})/R$ is taken for the ion heat diffusivity [2,3], where f is some function of $\gamma$, $\hat{s}$ and $\tau_{ZF}$. Here, $\gamma$ is the growth rate of the mode energy, $\hat{s}$ is the magnetic shear parameter and $\tau_{ZF}$ is so-called the decay time of zonal flows [4]. We need to study that which modes are destabilized to determine which models should be chosen for the turbulent diffusivities in transport codes. The GKV-X code solves the gyro-kinetic equation to examine Ion Temperature Gradient (ITG) modes and zonal flows in Large Helical Device (LHD) for the turbulent transport in helical plasmas [2]. For the first step, we perform the linear gyro-kinetic analysis by using GKV-X codes for ITG modes in the LHD high-$T_i$ discharge case of the shot number 88343, even if GKV-X codes retain the nonlinear characteristic. This is because the simulation cost of the linear analysis is extremely smaller than that of the nonlinear simulation [5]. The turbulent diffusivity is roughly determined by the linear growth rate and the wavelength according to the mixing length estimate in the gyro-kinetic simulation results. The calculation of the growth rate by use of the gyro-kinetic codes at each time step in the dynamical transport codes takes a high cost. Modeling of the ion heat diffusivity is necessary in terms of the significant parameter for the plasma instability, which is available in the dynamical transport codes. In this study, the significant parameter for the ITG instability is considered to be $L_{Ti}(=-T_i/T_i')$. The other parameters such as $L_n$ and the safety factor are fixed. The dependence of the zonal flow decay time $\tau_{ZF}$ on the function f is neglected in modeling $\chi_i$. The form for the ion heat diffusivity $\chi_i$ is derived. This form is used in the transport code to compare the simulation results with the radial profile for the ion temperature in LHD experimental results.

Firstly, the simulation of the linear analysis is done using GKV-X codes. The ITG instability is examined in the LHD high-$T_i$ discharge case of the shot number 88343. This simulation is for the three dimensional equilibrium field configuration with the major radius R=3.75m. We set $T_e=T_i$. The saturation level of the linear growth rate for the perturbation of the electrostatic potential is calculated. The value of the ion heat diffusivity $\chi_i/\chi_{GB}$ is evaluated as $\chi_i/\chi_{GB} = C\sum_{k_y}\gamma/k_y^2$, where $\chi_{GB}(=\rho_{ti}^2 v_{ti}/R)$ is the gyro-Bohm diffusivity, $k_y$ is the poloidal wavenumber and $\gamma$ is the linear growth rate for the ITG mode. We use the numerical factor C to match the simulation results with the experimental results and set C=1. To find the critical ion temperature gradient for the ITG mode, the dependence of $\chi_i/\chi_{GB}$ on the normalized ion temperature gradient $R/L_{Ti}$ is examined. The dependence of $\chi_i/\chi_{GB}$ on $R/L_{Ti}$ is examined with all plasma parameters except

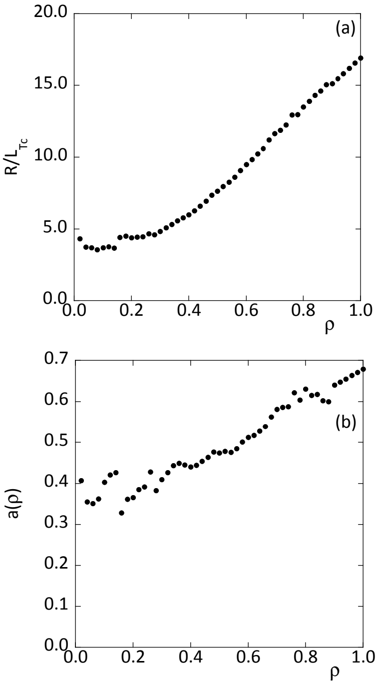

Fig. 1 The radial dependence of (a) the critical ion temperature gradient $R/L_{Tc}$ and (b) the slope a(ρ) in modeled ion diffusivity

the temperature gradient fixed at the stationary values for the density and the safety factor at fifty radial points. We model $\chi_i / \chi_{GB}$ as $\chi_i / \chi_{GB} = a(\rho)(R / L_{Ti} - R / L_{Tc})$, where $L_{Tc}$ is the normalized critical ion temperature gradient for the ITG instability and $\rho = r / a$. The slope $a(\rho)$ depends on the values of the normalized density gradient and the safety factor, which change due to the radial positions. The critical ion temperature gradient for the ITG mode, $R/L_{Tc}$ and the slope $a(\rho)$ in terms of $R/L_{Ti}$ are shown in Fig. 1.

Secondly, the transport dynamics is examined using the modeled ion turbulent diffusivity above, when the transport code [6] is performed. The neoclassical diffusion coefficient is derived from DGN/LHD database in the case of low-$\beta$ limit. The radial profile of the electric field is derived from the ambipolar condition. The three solutions of the ambipolar radial electric field are found in the radial region $0.25 < \rho < 0.80$. The positive radial electric field is chosen from three solutions of the ambipolar conditions in the radial region $0.25 < \rho < 0.80$. The plasma radial profiles except the ion temperature, such as the density, the electron temperature, the radial electric field and the safety factor are set to temporally be constant. The experimental result in #88343 at t=2.230s of LHD is used for the radial profiles of the density, the electron temperature, and the safety factor. The dynamics of the $T_i$ radial profile is simulated, by use of the transport code. The $T_i$ profile of the experimental results is used as an initial state for the dynamical transport simulation. We show the simulation results for the stationary ion temperature profile with the solid line in Fig. 2(a). The dashed line indicates the radial profile of $T_i$ in #88343 at t=2.230s of LHD. The simulation results for the radial $T_i$ profile can show the good agreement with one experimental result in #88343 at t=2.230s of LHD. The stationary radial profiles of the turbulent and neoclassical diffusivities are also shown in Fig. 2(b). The ITG mode is stabilized in two radial regions $0.0 < \rho < 0.25$ and $0.8 < \rho < 0.92$. The solid and dashed lines represent ion turbulent and neoclassical diffusivities. The turbulent transport is dominant compared with the neoclassical transport in the radial region where the positive electric field is chosen.

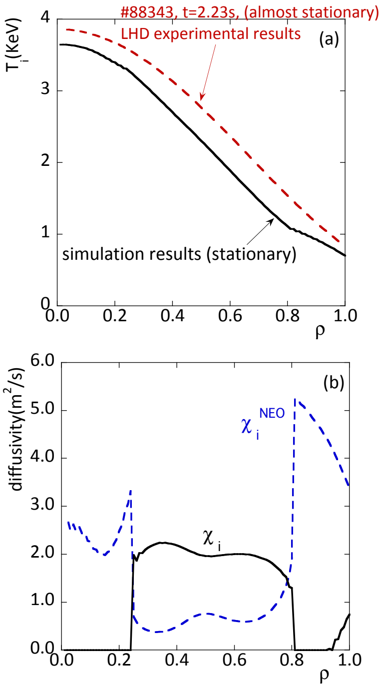

Fig. 2 Radial profiles of (a) the ion temperature and (b) the ion diffusivity

In this study, modeling of the ion heat diffusivity is done in terms of the scale length of the ion temperature gradient to introduce the ITG turbulence in the transport codes, especially in the LHD high-$T_i$ discharge case of #88343. Using the dynamical transport codes, we compared the simulation results using modeled ion turbulent heat diffusivity with an experimental result in the LHD high-$T_i$ case of #88343. We should compare the simulation results of the linear gyro-kinetic analysis with the results by use of the nonlinear analysis. Furthermore, the effect of zonal flows is necessary to be included. Modeling of the heat turbulent diffusivity will be done in more general cases. These are for the future studies.

## References

[1] A. Wakasa et al., 39th EPS Conference on Plasma Physics joint with the 16th International Congress on Plasma Physics, P2.028 (2012)
[2] M. Nunami et al., Physics of Plasmas **19**, 042504 (2012)
[3] J. W. Connor and H. R. Wilson, Plasma Phys. Control. Fusion **36**, 719 (1994)
[4] H. Sugama and T. -H. Watanabe, Physics of Plasmas **13**, 012501 (2006)
[5] M. Nunami et al., Physics of Plasmas **20**, 092307 (2013)
[6] S. Toda and K. Itoh, Plasma Phys. Contr. Fusion **44**, 325 (2002)

# Numerical analysis of neoclassical flow by the moment method at the NBI Plasma in Heliotron J

K. Nishioka[1], Y. Nakamura[1], S. Nishimura[2], H. Y. Lee[3], S. Kobayashi[4], T. Mizuuchi[4], K. Nagasaki[4], H. Okada[4], T. Minami[4], S. Kado[4], S.Yamamoto[4], S. Ohshima[4],S. Konoshima[4] and F. Sano[4]

[1]*Graduate School of Energy Science, Kyoto University* [2] *National Institute for Fusion Science*

[3] *Natural Science Research Institute, Korea Advanced Institute of Science and Technology,*

[4] *Institute of Advanced Energy, Kyoto University*

The investigation of the plasma flow and viscosity is important to understand the transport and stability of magnetically confined plasma. For the experimental effort, carbon parallel flow measurement has been carried out in many tokamak and stellarator/Heliotron devices, also in Heliotron J [1], based on the CXRS method. However, it is difficult for CXRS to measure the bulk ion flow velocity directly. Therefore, numerical method has important roles for the investigation of parallel flow and viscosity.

When we targeted the NBI plasma, we should take into account the existence of external momentum. When high energy neutrals are injected into plasma, parallel momentum was also injected. This external source affects the neoclassical transport matrix itself through the change in parallel momentum balance.

When fast ion exists, the general force balance equation is as follows [2,3];

$$\left[-\begin{bmatrix}\mathbf{M}_{\mathrm{a}} & 0 & \cdots & 0\\ 0 & \mathbf{M}_{\mathrm{b}} & \cdots & 0\\ \vdots & \vdots & \ddots & \vdots\\ 0 & 0 & \cdots & \mathbf{M}_{\mathrm{N}}\end{bmatrix}+\begin{bmatrix}\boldsymbol{\Lambda}_{\mathrm{aa}} & \boldsymbol{\Lambda}_{\mathrm{ab}} & \cdots & \boldsymbol{\Lambda}_{\mathrm{aN}}\\ \boldsymbol{\Lambda}_{\mathrm{ba}} & \boldsymbol{\Lambda}_{\mathrm{bb}} & \cdots & \boldsymbol{\Lambda}_{\mathrm{bN}}\\ \vdots & \vdots & \ddots & \vdots\\ \boldsymbol{\Lambda}_{\mathrm{Na}} & \boldsymbol{\Lambda}_{\mathrm{Nb}} & \cdots & \boldsymbol{\Lambda}_{\mathrm{NN}}\end{bmatrix}\right]\cdot\begin{bmatrix}\mathbf{U}_{\mathrm{a}}\\ \mathbf{U}_{\mathrm{b}}\\ \vdots\\ \mathbf{U}_{\mathrm{N}}\end{bmatrix}$$

$$=\begin{bmatrix}\mathbf{N}_{\mathrm{a}} & 0 & \cdots & 0\\ 0 & \mathbf{N}_{\mathrm{b}} & \cdots & 0\\ \vdots & \vdots & \ddots & \vdots\\ 0 & 0 & \cdots & \mathbf{N}_{\mathrm{N}}\end{bmatrix}\cdot\begin{bmatrix}\mathbf{X}_{\mathrm{a}}\\ \mathbf{X}_{\mathrm{b}}\\ \vdots\\ \mathbf{X}_{\mathrm{N}}\end{bmatrix}-\begin{bmatrix}\mathbf{Z}_{\mathrm{a}}\\ \mathbf{Z}_{\mathrm{b}}\\ \vdots\\ \mathbf{Z}_{\mathrm{N}}\end{bmatrix}\left\langle BE_{\parallel}\right\rangle-\begin{bmatrix}\mathbf{C}_{\mathrm{a}}\\ \mathbf{C}_{\mathrm{b}}\\ \vdots\\ \mathbf{C}_{\mathrm{N}}\end{bmatrix}\left\langle BF_{\mathrm{f}\parallel 1}\right\rangle$$

where $\mathbf{M}$ is $\left(j_{\max}+1\right)\times\left(j_{\max}+1\right)$ viscosity coefficient matrix, $\boldsymbol{\Lambda}$ is $\left(j_{\max}+1\right)\times\left(j_{\max}+1\right)$ friction coefficient matrix, $\mathbf{N}$ is $2\times\left(j_{\max}+1\right)$ matrix which indicates viscosity from radial potential gradient, $\mathbf{X}$ : drive force from pressure and temperature gradient, $\mathbf{Z}$ : momentum driven by parallel electric field, $\mathbf{C}$ : momentum transfer ratio to each particle specie and $\left\langle BF_{\parallel \mathrm{f}1}\right\rangle$ is the total parallel momentum input. The $j_{\max}$ is the order of Laguerre expantion. Our new term is the last term of right hand. We obtained parallel particle and heat flow $\mathbf{U}_{\mathrm{a}}$ by solving above simulatenous equation considering the effect of external momentum and finite radial electric field which satisfies ambipolar condition $\sum_{\mathrm{a}} e_{\mathrm{a}}\Gamma_{\mathrm{a}}=0$.

Numerical estimation by the moment method and CXRS measurement of the parallel $C^{6+}$ flow velocity in the standard (STD) and high gamma (HG) field on Heliotron J are shown in Figure 1(a) and (b).

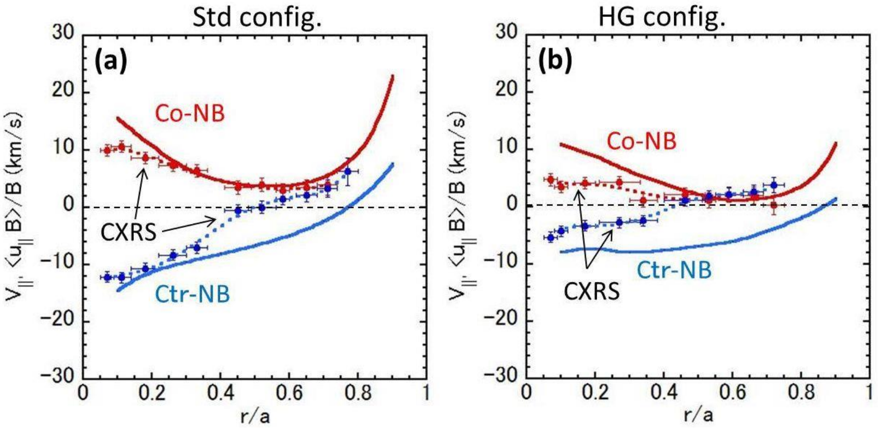

Fig. 1. Radial profiles of parallel $C^{6+}$ flow velocity measured by CXRS (dotted-lines) and of calculated neoclassical flow velocity (solid-lines) in STD configuration at (a) and HG configuration at (b).

These figures indicate that numerical estimation of carbon flow is consistent with the experimental result at both co- and counter- NBI plasma. In addition to this, we observed that HG configuration reduces $u_{||}$ by a factor of 1/2 that in STD configuration at central region both in measurement and calculation.

We show the parallel viscosity coefficient of $C^{6+}$ ion both in STD and HG configurations in Fig.2. This figure denotes that neoclassical $C^{6+}$ viscosity coefficient in HG configuration is much larger than that in STD configuration by the large parallel magnetic ripple depth. The detailed estimation of controllability of parallel plasma flow, and poloidal and toroidal viscosity of ions are the furure work.

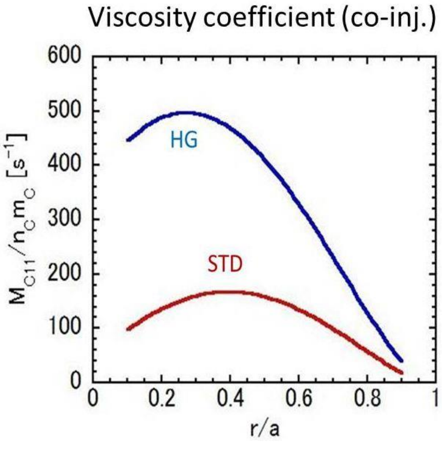

Fig. 2. Radial profiles of parallel $C^{6+}$ ion viscosity coefficients in STD and HG configurations

References

[1] H. Lee, et al. Plasma Phys. Ctr. Fusion **55** (2013) 035012

[2] N.Nakajima and M.Okamoto, J. Phys. Soc. Jpn. **61**, (1992), 833

[3] S. Nishimura, et al, Phys. Plasmas. **17**, 082510 (2010) , Phys. Plasmas. **18**, 069901 (2011)

# Integrated simulation of ELM control by Pellet Injection

N. Hayashi [1], N. Aiba [1], T. Takizuka [2], N. Oyama [1]

[1] JAEA, [2] Osaka Univ.

The energy loss caused by the edge localized mode (ELM) needs to be reduced for ITER operations with ELMy H-mode plasmas. The pellet injection is considered as one possible method to reduce the ELM energy loss by increasing the ELM frequency (so called ELM pacing). The ELM pacing requires the significant reduction of ELM energy loss, small impact on the plasma performance, and less particle fueling. The reduction of ELM energy loss by the pellet injection for ELM pacing has been studied by an integrated code suite TOPICS (it has been formerly referred to as TOPICS-IB [1]. Now it is simply referred to as TOPICS, since the core transport module which was called TOPICS has evolved integrating other functions and modules so as to represent the suite). TOPICS simulations showed that the energy absorption by pellet ablation clouds and the subsequent ExB drift can steepen the pressure gradient locally in the pedestal, which destabilizes high-n ballooning or intermediate-n peeling-ballooning modes and triggers an ELM, where n is the toroidal mode number [1]. It was also found that the ELM energy loss can be significantly reduced by the low-field-side injection of a pellet with about 1 % of pedestal particle content and a speed fast enough to approach the pedestal top when the pedestal pressure is about 95 % of natural ELM onset [2]. In this paper, we do simulations of JT-60U plasmas with various parameters and ITER plasmas of standard operation scenario, examine the effectiveness of the above suitable conditions for ELM pacing and evaluate the pellet particle content required for ELM pacing.

The pellet triggered ELM is investigated by TOPICS, which couples the core transport module with an MHD stability code MARG2D, a scrape-off-layer / divertor transport model D5PM and a pellet model APLEX taking account of the *E*x*B* drift of pellet plasma cloud [1]. The core transport module is based on the 1.5D core transport code, which solves the 1D transport and current diffusion equations on the normalized toroidal flux coordinate, and the Grad-Shafranov equation of MHD equilibrium on the 2D plane. Particle and thermal diffusivities consist of neoclassical and anomalous ones where the anomalous diffusivities are given as empirical formulas. In order to produce the H-mode pedestal, the transport near the edge is reduced to the neoclassical value calculated by the matrix inversion method with a prescribed characteristic width of pedestal. The ELM model is developed by coupling TOPICS with MARG2D. In the present simulation, the stability of n = 1-50 modes are examined at given time-intervals. When unstable modes appear, an ELM is assumed to occur. ELM enhanced diffusivities are added on the basis of eigenfunction profiles of unstable modes, where the maximum value is given as a parameter. The ELM enhanced transport is maintained for a time interval given as a parameter. D5PM is based on time-dependent fluid equations. Particle flux and heat fluxes across the separatrix obtained in TOPICS are used as inputs and D5PM calculates the SOL density and temperatures at the separatrix, which are used as boundary conditions in TOPICS. The particle balance in the whole regions is modeled by integrating neutral models with TOPICS and D5PM. APLEX assumes a sphere pellet and simulates the pellet ablation, ExB drift of ablated and detached plasma cloud, cloud energy absorption from the background plasma and deposition to the background plasma. The pellet model APLEX takes into account 3D geometry, in which plasma clouds produced from a pellet drift along the major radius and expand along magnetic field lines. It is worth noting that, during the pellet ablation and further drift, we use the 1.5D transport code for the profile evolution of background plasma (1D transport and 2D MHD equilibrium), and the linear MHD stability code MARG2D to check the stability of the 2D MHD equilibrium and to model ELMs in the 1D transport. In our study, we fix the model parameters such as in the ELM model and examine the dependence appearing in simulation results.

JT-60U parameters are the same as in previous studies [1,2], typical ones in ELMy H-mode experiments. ITER parameters are for standard scenario and the ELM model parameters are the same as in JT-60U simulations, except for four times larger diffusivities because the characteristic length, the pedestal width, is roughly doubled in the real coordinate. The pedestal width almost agrees with the EPED prediction. Figure 1 shows the ELM energy loss $\Delta W_{\mathrm{ELM}}$ normalized by the pedestal stored energy $W_{\mathrm{ped}}$ as a function of pellet position at the ELM onset $\rho_{\mathrm{pel,onset}}$ for JT-60U and ITER simulations, where mode locations are also shown. As the same as the previous result, with the suitable conditions, a pellet can significantly reduce the

ELM energy loss by penetrating deeply into the pedestal and triggering high-n ballooning modes localized near the pedestal top. Without the suitable conditions, the pellet triggers lower-n modes with wide mode width before the pellet approaches the pedestal top, and enhances the ELM energy loss, which becomes comparable to the natural ELM level at the maximum. In all simulations with the suitable conditions, a similar level of reduced energy loss is obtained. Thus, the effectiveness of suitable conditions has been confirmed. Figure 2 shows the relation between the pellet particle content $N_p$ (normalized by the pedestal particle content $N_{ped}$) required for ELM pacing and the variation of normalized pressure gradient $\Delta\alpha$ (normalized by the critical gradient $\alpha_{cr}$ of ideal ballooning mode (IBM)) required to destabilize the high-n ballooning modes. Here, the IBM stability can be used to judge the onset of high-n ballooning modes [3]. The pellet particle content required for ELM pacing is larger for the pedestal plasma with higher density and farther from the IBM stability boundary near the pedestal top. For ITER, the required pellet particle content is within the range of present empirically-designed value for the pellet to reach the pedestal top [4] and thus our evaluation gives the physical background to the design.

**References**

[1] N. Hayashi et al, Nucl. Fusion **51** (2011) 103030.
[2] N. Hayashi et al, Nucl. Fusion **53** (2013) 123009.
[3] N. Hayashi et al, Nucl. Fusion **52** (2012) 114002.
[4] A. Loarte et al, 24th IAEA FEC, San Diego, 2012

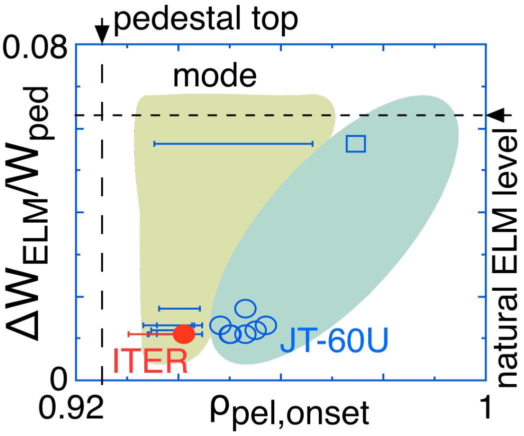

*FIG.1. Dependence of $\Delta W_{ELM}/W_{ped}$ on pellet position at ELM onset for JT-60U simulations (blue open) and an ITER simulation (red closed), where horizontal solid lines denote mode locations, circle symbols do results with suitable conditions of pellet injection for ELM pacing, a square symbol does an example without suitable conditions and shaded regions denote other results in JT-60U. Vertical and horizontal dotted lines denote pedestal top position and $\Delta W_{ELM}$ of natural ELM level, respectively.*

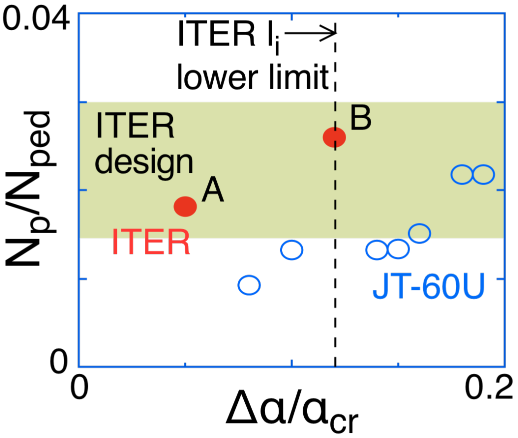

*FIG.2. Dependence of $N_p/N_{ped}$ on $\Delta\alpha/\alpha_{cr}$ for JT-60U (blue open) and ITER (red closed) simulations, where shade region denote pacing pellet size of present ITER design [3]. In ITER simulations, normalized internal inductance $l_i$ is varied from a typical value to ITER lower limit (A→B).*

# ペレット入射プラズモイドのドリフト機構のモデリングと実験との比較
# Study on Drift Displacement of Pellet Plasmoid and Comparison to Experiments

松山顕之
Akinobu MATSUYAMA

日本原子力研究開発機構
Japan Atomic Energy Agency

## 1. Introduction

Historically, an issue for pellet fuelling was to develop high-speed injectors that are capable of injecting pellets successively with the speed of 5-10 km/s. At present, a more favorable scheme is available with the high-field side (HFS) pellet injection. Injecting the pellet from the HFS was found to improve the fueling efficiency as compared to a conventional low-field side (LFS) injection scheme. In such an injection configuration, a plasma cloud surrounding the pellet drifts spontaneously towards the plasma core, and provides deep deposition of pellet particles without fueling degradation due to high additional heating power. Therefore, the HFS injection is now considered to be the most promising technique for fuelling tokamak reactors, allowing use with the injection velocity of < 1 km/s, which is realized by the present technology.

To predict the pellet fueling properties in present tokamaks and future reactors, simulation models for the pellet injection especially taking into account the drift displacement of particle deposition have been developed. Using the HPI2 code [1], the simulation of pellet particle deposition has been compared to experimental results in present tokamaks, such as JET, Tore-Supra, and DIII-D. However, the validation of existing drift models against experiments is still under discussion. As an attempt for extending such validation study, we here investigate the pellet particle deposition in magnetic configurations other than tokamaks such as RFPs and helical devices. This is a good test for validating if present drift models can reproduce the drift displacement taking into account differences of the magnetic geometries in these devices. For this purpose, we extend the drift models implemented in the HPI2 code and compare the simulation data against the pellet injection experiments in the Large Helical Device (LHD) [2].

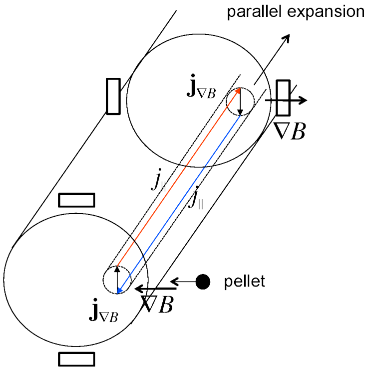

Fig. 1 Schematic picture of the suppression of polarization current by plasmoid internal current in a straight helical geometry.

## 2. Drift Modeling of Pellet Plasmoid

Helical devices possess three-dimensional magnetic geometries, which exhibit intrinsically different characteristics from that of axisymmetric tokamaks. We consider two important characteristics that affect the drift displacement: (1) steep magnetic field gradient that varies with the characteristic scale of a plasma minor radius, depending on the distance from the external helical coils, and (2) a helical modulation of the magnetic field with short connection lengths, where the direction of the magnetic field gradient varies rapidly when plasmoids expand in the toroidal direction. Because of the property (1), the plasmoid drift acceleration at the pellet injection location is much stronger than what is expected for tokamaks by up to a factor of the aspect ratio. Nevertheless, the plasmoid internal current suppresses this strong drift displacement as soon as the plasmoid expands over the connection length. The latter was originally considered for tokamak geometry [3], which we extend to general magnetic configurations and implement in the HPI2 code. Figure 1 shows a schematic picture of this effect in a straight helical configuration. At the pellet injection point on the low field side, the magnetic field gradient directs inwardly, but after the plasmoid expends at the sonic velocity over a half-period of the helical magnetic field, the gradient at the end of the plasmoid is seen to direct outwardly. For the divergence-free condition of the plasmoid internal current to be satisfied, the field-aligned current connects these two opposite currents. As a result, field-aligned currents suppress the drift acceleration significantly, which is understood in the analogy to the Pfirsch-Schlüter current in the MHD equilibrium theory. We found that the extended HPI2 code taking into account this drift suppression effect well reproduces the drift velocity and experimental deposition in the LHD [2].

## 3. High-Field Side Injection in Large Helical Device

A clear demonstration of the effect of different magnetic geometries between tokamaks and helical devices has been observed experimentally for the HFS injection. Surprisingly, the HFS injection in the LHD did not exhibit the improved capability of fuelling, and even the outward drift displacement was observed [4]. Our main result is that this unexpected result for the HFS injection can be understood from the effect of field-aligned current discussed in the previous section, if one takes into account realistic magnetic field geometry including the magnetic hill in the outer plasma region of the LHD. Figure 2 shows the effect of magnetic well/hill structure on the particle deposition, simulated by the extended HPI2 model. If we change the magnetic-field configuration from that with the magnetic well to that with the magnetic hill, it can be seen that for the HFS injection, the outward displacement as compared to the ablation profile is obtained. Even when one injects the pellet from the HFS and the local drift velocity directs inwardly, the drift suppression due to the field-aligned current occurs. After the compensation of a local drift velocity, the drift direction is dominated by whether the magnetic field in the deposition region possesses magnetic well or hill structure. This is because the drift due to the averaged magnetic curvature is unaffected by the field-aligned current. We mention that the drift displacement due to the magnetic well discussed here is correlated to a particular importance of the interchange mode in heliotron devices. As a whole, the LHD results are seen to be in contrast to what is expected for tokamaks, where the direction of drift displacement is dominated mainly by a local magnetic curvature (ballooning-like drift motion). The connection length should dominate a relative importance between such interchange and ballooning drift motion; this idea extends the original model discussed by Rozhansky, *et al.* [3], and is useful for understanding the drift displacement in different magnetic configurations. We applied the extended HPI2 code for experimental parameters of [4] and found that the simulation data well reproduces observed outward displacement with respect to both the peak location and the density increase.

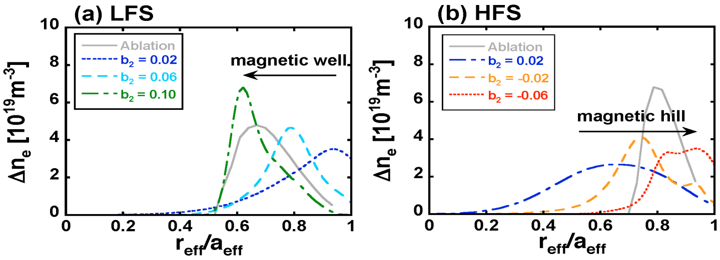

Fig. 2 Effect of edge magnetic field structure on the deposition profile: (1) LFS injection case and (2) HFS injection case when the magnetic field configuration is varied from that with the magnetic hill to that with the magnetic well.

## 4. Conclusion

In this work, the pellet fueling models are extended for understanding the drift displacement in different magnetic configurations, i.e., tokamaks, RFPs and helical devices. The extended HPI2 code was compared with the experimental results in the LHD. An essential point is to include the effect of field-aligned current that compensates the local drift acceleration, which yields the long-term drift depending on whether the magnetic configuration possesses magnetic well or hill structure. The developed code has been confirmed, for the first time, to well reproduce main characteristics of the pellet fueling in the LHD.

Further code validation will be important, in particular, concerning the effect of low-order rational surfaces [5]. In the previous work, the correlation between the deposition peak and the position of low-order rational surfaces has been reported for tokamaks [6], and it will affect quantitative prediction of the fueling the reactors. For this reason, testing this effect in the LHD is of particular interest, where the strong drift damping due to the $q$ = 1 surface at the deposition region is suggested ($q$: safety factor).

## References

[1] F. Koechl, *et al.*, Submitted to Nucl. Fusion.
[2] A. Matsuyama, *et al.*, Nucl. Fusion 52, 123017 (2012).
[3] V. Rozhansky, *et al.*, Plasma Phys. Control. Fusion 46, 575 (2004).
[4] H. Yamada, et al., Plasma Phys. Control. Fusion **43**, A55 (2001).
[5] B. Pégourié and M. A. Dubois, Nucl. Fusion, **29**, 745 (1989).
[6] N. Commaux, *et al.*, Nucl. Fusion **50**, 025011 (2010).

# Radio-frequency sheath-plasma interactions in the ion cyclotron range of frequencies

Haruhiko Kohno[1,*], James R. Myra[2] and Daniel A. D'Ippolito[2]

[1]Department of Mechanical Information Science and Technology, Kyushu Institute of Technology
680-4 Kawazu, Iizuka, Fukuoka 820-8502, Japan
[2]Lodestar Research Corporation, 2400 Central Avenue P-5, Boulder, Colorado 80301, USA
*Author to whom correspondence should be addressed E-mail: kohno@mse.kyutech.ac.jp

## ABSTRACT

A numerical code that solves self-consistent radio-frequency (RF) sheath-plasma interactions in the ion cyclotron range of frequencies (ICRF) is developed based on a finite element technique. The present code solves for waves in the edge plasma subject to a sheath boundary condition. In this two-dimensional study, it is found that rapid variation of conditions along the sheath surface promotes coupling of the incident RF branch to a short-scale-length sheath-plasma wave (SPW). The SPW propagates along the sheath surface in a particular direction dictated by the orientation of the magnetic field with respect to the surface, and the wave energy in the SPW accumulates near places where the background magnetic field is tangent to the surface. This phenomenon is expected to be relevant to the formation of localized hot spots on the bounding surfaces, which are commonly observed on powered ICRF antennas.

**Keywords**: Radio-frequency sheaths, Plasma waves, Magnetic confinement fusion, Finite element method

## 1. INTRODUCTION

Radio-frequency (RF) waves in the ion cyclotron range of frequencies (ICRF) have been successfully applied to various heating experiments in fusion plasmas. However, it has been revealed by experimental and theoretical studies that deleterious edge plasma interactions can occur due to various nonlinear mechanisms [1]. One of the most important nonlinear effects is RF sheath formation, in which the sheath potential on the walls and limiters of the tokamak device is enhanced by the ICRF waves. RF sheath formation causes various problems including impurity generation by enhanced sputtering and power dissipation in the scrape-off layer (SOL), leading to local hot spots and reduced power. Because sheaths occur on the scale of the Debye length, which is much smaller than domain sizes or RF wavelengths of interest for fusion applications, approximate RF sheath boundary condition (sheath BC) approaches have been developed [2,3]. These approaches effectively treat the sheath as a thin vacuum layer, and thus capture the important effect of sheath capacitance on the boundary. In addition, a finite element procedure employing this sheath BC has recently been developed by the authors for the purpose of solving self-consistent RF sheath-plasma interactions in the ICRF [4]. In this short paper, we will briefly summarize our recent finding of an important role in governing the distribution of wave energy and induced potentials along the sheath surface subject to rapid variation of conditions [5].

## 2. MATHEMATICAL MODELING

The governing equation for plasma waves in the SOL is a combined form of Maxwell's equations described as

$$\nabla \times \nabla \times \mathbf{E} - \frac{\omega^2}{c^2}\boldsymbol{\varepsilon}\cdot\mathbf{E} - \mathrm{i}\omega\mu_0\mathbf{J}_{\mathrm{ext}} = \mathbf{0}, \tag{1}$$

where the electric field $\mathbf{E}$ and the external current $\mathbf{J}_{\mathrm{ext}}$ vary on the RF time scale. Here, $\omega$ is the applied ICRF wave frequency, $c$ is the speed of light, and $\mu_0$ is the permeability in vacuum. The dielectric tensor $\boldsymbol{\varepsilon}$ is given based on the cold plasma model. At the metal wall, the sheath effect is taken into account by means of a sheath BC, which is written as follows:

$$\mathbf{E}_{\mathrm{t}} = \nabla_{\mathrm{t}}\left(\frac{\Delta_{\mathrm{sh}}}{\varepsilon_{\mathrm{sh}}}D_{\mathrm{n}}\right). \tag{2}$$

Here, $\Delta_{\mathrm{sh}}$ is the time-averaged sheath width, $\varepsilon_{\mathrm{sh}}$ is the dielectric constant in the sheath, $D_{\mathrm{n}}$ is the component of the electric displacement normal to the sheath, and the subscript t denotes the two components tangential to the boundary. For the linear case, the sheath width is expressed as follows:

$$\Delta_{\mathrm{sh}} = C_{\mathrm{th}}\lambda_{\mathrm{De}}, \tag{3}$$

where $\lambda_{\mathrm{De}}$ is the electron Debye length. The coefficient $C_{\mathrm{th}}$ is a function of the surface contact angle of the magnetic field line (see [5] for more detail).

## 3. RESULTS AND DISCUSSION

In the present finite-element numerical analysis, we consider solutions of the sheath-plasma interactions for spatially varying background magnetic fields whose flux surfaces have tangency points at a boundary. This magnetic field configuration actually happens with limiter surfaces in a tokamak. Figure 1 shows the filled contour plot of $E_{\|}$, which is the electric field component parallel to the magnetic field line. Here, the antenna and magnetic field lines are also superimposed on the plot. Since this is a plot of $E_{\|}$, the fast wave contribution is considered to be negligible. It is observed that the slow wave (SW) propagates along the magnetic field lines although it is evanescent from the antenna position. In addition, the sheath-plasma wave (SPW) is generated on the sheath surface between the "convex" flux-surface tangency point ($y$ = 0.3 m) and the intersection point ($y$ = 0.6 m) of a magnetic field line penetrating the antenna and the wall (hereafter, the flux-surface tangency points from which the magnetic field lines inside the plasma are seen as convex and concave curves are simply called the convex and concave tangency points at the sheath surface, respectively). While the present geometry is too simple to apply directly to a tokamak, in general the complex magnetic fields of shaped diverted plasmas, and realistic vessel walls can exhibit both types (convex and concave) of interactions. The generation of the SPW is also confirmed in Fig. 2, which shows the variations of the real part of the parallel electric field component along the sheath surface for two different boundary conditions at the right wall; here, the result obtained by imposing the conducting-wall BC is added for comparison. It is seen that the SPW is generated only by imposing the sheath BC. Furthermore, it is important to notice that the SPW is driven in the narrow region within which the magnetic field lines connect the antenna to the wall and accumulation of its energy occurs at the convex tangency point. It has been clarified through the analysis of the electromagnetic SW-SPW dispersion relation that the wave mode propagates energy away from the concave point and towards the convex point [5]. The dramatic slowing of the group velocity near $y$ = 0.3 m leads to an accumulation of wave energy there.

In recent Alcator C-Mod experimental work, large plasma potentials (~ 100 V) were found on field lines connecting the emissive probe to a nearby plasma limiter [6]. This plasma potential rose rapidly in the vicinity of the limiter tip and then decayed exponentially along the major radius direction behind the limiter tip. The wave energy deposition at the magnetic field tangency point on the sheath surface, which has been discovered in the present work, may be the cause of these experimental results. However, of course, further work is necessary to establish this point.

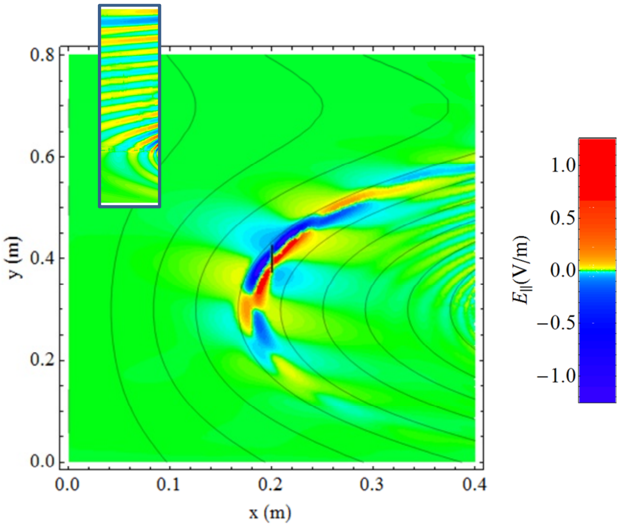

FIG. 1. Filled contour plot showing the distribution of the electric field component parallel to the magnetic field lines.

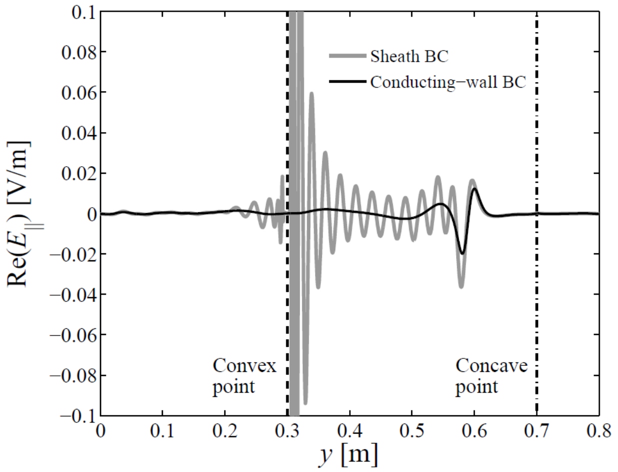

FIG. 2. Plot of the real part of the parallel electric field component along the sheath surface with a comparison to the result for the conducting-wall BC.

## REFERENCES

[1] J. R. Myra, D. A. D'Ippolito, D. A. Russell, L. A. Berry, E. F. Jaeger, and M. D. Carter, Nucl. Fusion **46**, S455 (2006).

[2] J. R. Myra, D. A. D'Ippolito, and M. Bures, Phys. Plasmas **1**, 2890 (1994).

[3] D. A. D'Ippolito and J. R. Myra, Phys. Plasmas **13**, 102508 (2006).

[4] H. Kohno, J. R. Myra, and D. A. D'Ippolito, Comput. Phys. Commun. **183**, 2116 (2012).

[5] H. Kohno, J. R. Myra, and D. A. D'Ippolito, Phys. Plasmas **20**, 082514 (2013).

[6] R. Ochoukov, et al., J. Nucl. Mater. **438**, S875 (2013).

# One-Dimensional Transport Analysis of ECRH Assisted Start-up in JT-60SA

K. Hada[a], K. Nagasaki[b], K. Masuda[b], S. Ide[c] and A. Isayama[c]

[a]*Graduate School of Energy Science, Kyoto University, Japan*
[b]*Institute of Advanced Energy, Kyoto University, Japan*
[c]*Japan Atomic Energy Agency, Naka, Ibaraki, Japan*

E-mail address: hada.880@iae.kyoto-u.ac.jp

There is a considerable interest in plasma start-up assisted by electron cyclotron resonance heating (ECRH) in superconducting tokamaks because available loop voltage is generally low compared with conventional normal-conducting tokamaks. In JT-60SA superconducting tokamak ($R_0$ = 2.96 m, $a$ = 1.18 m, and $B_T$ = 2.25 T), which is now under construction in JAEA [1], the toroidal electric field for plasma breakdown is limited up to 0.5 $V \cdot m^{-1}$. This may make it difficult to start up plasmas if the first wall is not in good condition. On JT-60SA, a 7 MW ECRH system with multi frequency (110 GHz and 138 GHz) gyrotrons is equipped for heating and current drive as well as for plasma start-up. The main purposes of this paper are to examine the conditions for the reliable start-up and to understand the dominant physical process in the plasma start-up phase. We have previously studied the plasma start-up assisted by ECRH in JT-60SA using a zero-dimensional (0-D) model [2]. The calculation using JT-60U parameters qualitatively reproduces the time evolution of the experimental results. However, the 0-D model is not enough to investigate the plasma start-up assisted by 2nd harmonic X-mode ECRH in large device such as JT-60SA. Hence, we are developing a one-dimensional (1-D) model. In order to consider the change in ECRH absorption power with time evolution of electron temperature and density, we consider the ECRH absorption efficiency. The 1-D model consists of energy transport equations for electrons and hydrogen ions, particle transport equations for electrons and hydrogen atoms, and toroidal current equation. In this model, we assume a cylindrically symmetrical plasma, a fixed plasma boundary, and that peak of ECRH absorption is located on axis. Figure 1. shows that the threshold ECRH power for plasma start-up is observed, the threshold ECRH power of around 1 MW is required to start up the plasmas for $n_H = 3.0 \times 10^{18}\ m^{-3}$, error field $B_{err}$ of about 1 mT, and EC beam radius of about 5 cm. This indicates a promising outlook for a reliable start-up in JT-60SA for a good wall condition. In case of low initial neutral density, we can start up plasmas without ECRH. However, another physical process is important in low initial neutral density, that is, we have to consider the generation of runaway electron causing direct loss. Figure 2. shows that the threshold ECRH power increases with error field ($B_{err}$ up to around 7 mT). This results suggests that the optimized magnetic field control may be necessary for the reliable start-up because the error

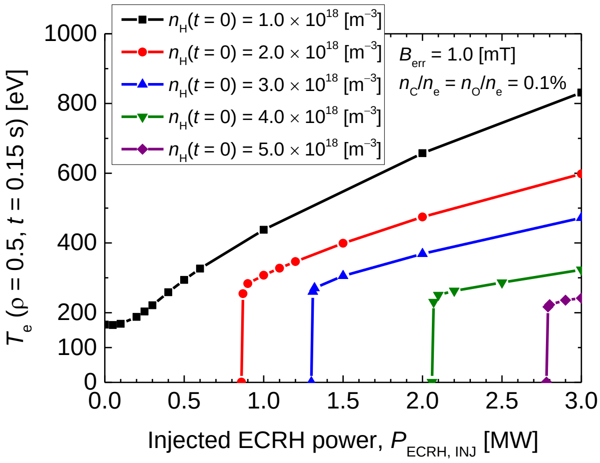

Fig 1. Dependence of electron temperature at ρ = 0.5 and $t$ = 0.15 s on initial neutral density and injected ECRH power.

field generated by induced current in passive structures such as vacuum vessel, stabilizing plate, port, and cryostat is estimated around 5-10 mT without optimized magnetic field control [3]. Figure 3. shows a time evolution of electron density, electron temperature, toroidal current, and electron power source and loss terms. This 1-D analysis provides an insight into the dominant physical process as follows. After the loop voltage is turned on, electron and ion densities gradually increase; therefore, ionization and equipartition losses become dominant. After ECRH injection, electron density promptly increases, nevertheless electron temperature still remains low. When hydrogen atoms are fully ionized, ECRH absorption efficiency is improved and electron temperature rises. This leads to a positive feedback, as a result, electron temperature drastically rises. The error field loss becomes dominant due to high electron temperature until the poloidal magnetic field generated by the plasma current exceeds the error field. This is considered to be a reason for the ECRH power threshold noted above to exist.

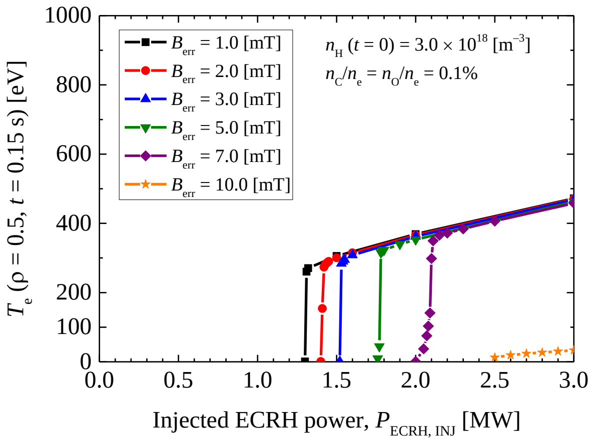

Fig 2. Dependence of electron temperature at ρ = 0.5 and *t* = 0.15 s on error field and injected ECRH power.

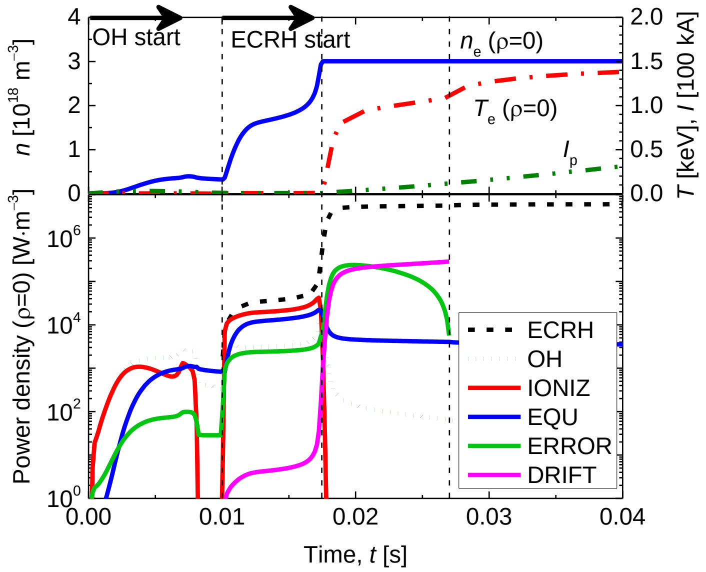

Fig 3. Time evolution of electron density and temperature, toroidal current, and electron power source and loss terms.

[1] S. Ishida *et al.*, Nucl. Fusion, **51** (2011) 094018

[2] K. Hada *et al.*, J. Plasma Fusion Res. **7**, (2012) 2403104

[3] M. Matsukawa *et al*, J. Plasma Fusion Res. **9**, (2010) 264

# Enhanced Neo-classical Resistivity Due to the m/n = 1/1 MHD-mode Deformation of Central Core Plasma Column for Tokamak Hybrid Scenario

T. Takizuka

Graduate School of Engineering, Osaka University

Hybrid scenario is planned for ITER to test the various engineering components towards DEMO with high reliability, high neutron fluence and long pulse length [1,2,3]. This scenario is the combination of the inductive current drive and the non-inductive current drive, and the q profile is of the weak magnetic shear. The fraction of the non-inductive current including the bootstrap current is expected to be 40~60%. Physical features of the hybrid scenario have been studied experimentally in the world. It was reported that the concentration of the current density peculiar to the inductive discharges was much smaller than that of simple estimation. DIII-D paper considered that this anomaly was caused by the hyper resistivity (see [4,5]) [6]. JT-60U paper showed similarly that the current concentration was smaller than the estimation [7]. Afterwards JT-60U report considered a possible reason, i.e., the enhanced electric resistivity was increased in the central region by the peaking of effective charge $Z_{\mathrm{eff}}$ with the accumulation of tungsten impurity [8].

We recently presented a new model of the physical mechanism on the reduction of the current concentration [9]. According to a JT-60U paper [7], there existed the $n = 1$ MHD activity (different from the neo-classical tearing mode) in hybrid-scenario discharges. The measured fluctuation of the electron temperature was large in the central region. This MHD activity can be the internal kink mode with a poloidal mode number $m = 1$ and a toroidal mode number $n = 1$, which becomes unstable for higher poloidal beta value ($\beta_{\mathrm{p}} \sim 1$) [10]. This mode brings the $m/n = 1/1$ kink deformation of the central plasma column between the magnetic axis with $q(0) < 1$ and a magnetic surface with $q \sim 1$. We assume a simple form of the finite normalized-amplitude of the deformation, $\xi = \xi_{\max} - \rho/2$ in a region $0 < \rho < \rho_{\mathrm{b}} = 2\xi_{\max}$, so that magnetic surfaces do not overlap. In the central core of a tokamak plasma with such an MHD deformation, trapped particles can exist even on the magnetic axis. The effective inverse aspect ratio becomes $\varepsilon_{\mathrm{eff}} = \varepsilon_{\mathrm{a}} (\rho + \xi)$ at the normalized minor radius $\rho$, and the neo- classical resistivity becomes as large as $\eta_{\mathrm{NC}} \approx \eta_{\mathrm{S}} / \{1 - (2\varepsilon_{\mathrm{eff}})^{1/2}\}$ in the central region ($\varepsilon_{\mathrm{a}}$ : inverse aspect ratio at the plasma surface, $\eta_{\mathrm{S}}$ : Spitzer resistivity).

In order to compare the present model with the experimental measurements, it is necessary to take into account of the finite-deformation effect on the diagnostics of poloidal magnetic field $B_{\mathrm{p}}$. The measured $B_{\mathrm{p}}$ value oscillates in time due to the toroidal rotation of the mode. Its time average $<B_{\mathrm{p}}>$ has been reported as the measured $B_{\mathrm{p}}$, but it is smaller than the true $B_{\mathrm{p}}$ on a magnetic surface. Based on the result of E48158 at $t = 27$s in JT-60U paper [7], we revise the measured data, poloidal magnetic field $B_{\mathrm{p}}$ and electron temperature $T_{\mathrm{e}}$, to the functions of $\rho$.

A trial function for the current density profile is introduced inside $0 < \rho < \rho_b$, $J_{tf}(\rho) = J_{ex}(\rho_b) \times (1 - k^2\rho^2) / (1 - k^2\rho_b{}^2)$, where $J_{ex}$ is the experimental function given in [7] and the $k^2$ value is determined so that the total current is constant. By changing the magnetic-axis displacement $\xi_{max}$ as a parameter, we reconstruct $J(\rho)$, $B_p(\rho)$, and $<B_p>$. When we put $\xi_{max} \approx 0.28$, we obtain a reconstructed $<B_p>$ profile very similar to the measured $B_p$ profile. Figure 1 shows the reconstructed $J(\rho)$ of the standard convex profile (red solid line) in contrast to the hollow profile of $J_{ex}(\rho)$ (blue circle chain). The central value $J(0)$ is 1.35 times larger than $J_{ex}(0)$.

The neo-classical resistivity $\eta_{NC}(\rho)$ is calculated from the reconstructed $T_e$ profile and the enhancement effect by $\varepsilon_{eff}$ assuming the uniform $Z_{eff}$. We estimate a current density profile $J_{cal}(\rho) \propto 1/\eta_{NC}(\rho)$ immediately (purple broken line in Fig. 1), and compare it with the reconstructed $J(\rho)$. They agree well with each other. The enhancement of neo-classical resistivity is important. If this enhancement is not taken into account, the estimated $J$ profile is very peaked near the magnetic axis as shown by a purple dotted line.

The $q$ profile is of the normal shear with $q(0) \approx 0.8$ in contrast to the reported $q_{ex}$ profile of the weak reversed shear with $q_{ex}(0) \approx 1.1$. This result is consistent with the assumption that the central core plasma column is deformed by the $m/n = 1/1$ internal kink mode. Present model can be valid to predict the $J$ profile for the hybrid scenario, and has to be applied to the integrated transport simulation.

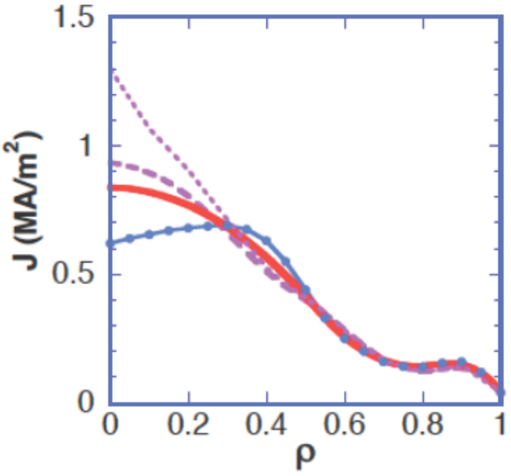

**Figure 1.** Radial profiles of current density $J(\rho)$ for JT-60U hybrid scenario. Experimentally reported $J_{ex}$ (blue circle chain), reconstructed $J$ (red solid line), calculated $J_{cal}$ (purple dashed line) and calculated one without enhanced neo-classical resistivity (purple dotted line).

[1] C. Gormezano et al., Nucl. Fusion **47**, S285 (2007).

[2] A.C.C. Sips et al., Plasma Phys. Control. Fusion **47**, A19 (2005).

[3] X. Litaudon et al., 2013 Nucl. Fusion **53**, 073024 (2013).

[4] A.H. Boozer, J. Plasma Phys. **35**, 133 (1986).

[5] H.L. Berk et al., “Hyper-resistivity Theory in a Cylindrical Plasma”, LLNL Report UCRL-ID-142741 (2001).

[6] T.A. Casper et al., Nucl. Fusion **47**, 825 (2007).

[7] N. Oyama et al., Nucl. Fusion **49**, 065026 (2009).

[8] T. Suzuki, private communication; T. Suzuki et al., “q-profile in Long-pulse Hybrid Discharge in JT-60U”, 6th ITPA IOS TG Meeting (2011).

[9] T. Takizuka, proc. 30th annual meeting JSPF, Tokyo (2013) 5aE39P: www.jspf.or.jp/jspf_annual2013/jspf30/pdf/05aE39P.pdf.

[10] S. Tokuda et al., Nucl. Fusion **22**, 661 (1982).

# Development of implicit MHD code

M. Sato, N. Nakajima, K.Y. Watanabe, Y. Todo and Y. Suzuki
National Institute for Fusion Science

As the beta value increases in LHD (Large Helical Device) plasmas, the Shafranov shift becomes large and the magnetic well is formed in the core region and the Mercier unstable region shifts form the core region to the peripheral region. Thus, the pressure driven MHD instabilities are theoretically unstable in the peripheral region for high beta LHD plasmas. On the other hand, high beta plasmas with about 5% of the volume averaged beta value are routinely obtained in the LHD experiments. This implies that nonlinear saturation level of the pressure driven modes is low enough to maintain such high beta plasmas. In this study, the linear properties and nonlinear phenomena of the pressure driven modes for high beta LHD plasmas have been investigated by MHD simulation in order to understand why high beta plasmas are stably obtained in LHD.

The MHD simulation has been carried out for three MHD equilibria with $\beta_0$ =7.4%, 9.4% and 11% by using the MIPS code (MHD Infrastructure for Plasma Simulation)[1] which solves the full MHD equations in the cylindrical coordinates. Here $\beta_0$ is the central beta value. The MHD equilibira are constructed by HINT2 code[2]. For these MHD equilibria, the ballooning modes extending into the plasma peripheral region with a chaotic magnetic field are destabilized. Since the linear growth rate decreases as the magnetic Reynolds number increases, the unstable modes are considered to be resistive modes. In the nonlinear phase, the core region comes under the influence of the instabilities and the central pressure decreases (Fig.1). There is a tendency that modes are suppressed as the beta value and/or magnetic Reynolds number increase, which is consistent with a result that high beta plasmas enter the second stable region of the ideal ballooning modes as beta increases [3] and remaining destabilized ballooning modes are considered to be resistive type.

In the MIPS code, the fourth-order explicit Runge-Kutta method is used for the time integration. The explicit time integration method has the problem of the CFL condition where the interval of the time step is limited by the fastest physics phenomenon. For extending the MIPS code to treat the free-boundary problem using the pseudo-vacuum plasma model, the initial density profile should be small in the pseudo-vacuum region. In the pseudo-vacuum region, the Alfven velocity increases so that the problem of the CFL condition becomes increasingly serious. In order to solve this problem, we are developing new MHD code using implicit time integration method. In the implicit time integration method, the interval of the time step is not limited by the CFL condition so that the simulation can be done using the large interval of the time step. For the first step of the developing of implicit MHD code, linear MHD code in two-dimensional xy-space has been developed in order to evaluate of the basic techniques for the implicit solver. In the implicit MHD code, the fourth-order finite difference method is used for the spatial derivatives and the first-order implicit Euler method with the Kryolv method is used for the time integration. In order to improve the convergence of the Krylov metod, the physics-based preconditioning[4] is introduced. The physics-based preconditioning method can improve the convergence of the Kryolov method by transforming the hyperbolic problem into the parabolic problem using the Schur decomposition. In order to check the effectiveness of the physics-based preconditioning, the dependence of the iteration number of the convergence of the Krylov method on the peripheral plasma density has been investigated using the two-dimensional implicit linear MHD code. When the physics-based preconditioning is not used, the iteration number for the convergence significantly increases as the peripheral plasma density decreases. On the other hand, for the implicit code with the physics- based preconditioning, the dependence of the iteration number on the peripheral plasma density is weak so that the physics-based preconditioning seems to be effective for the free-boundary problem. The extension of the two-dimensional implicit MHD code to three-dimensional is under development.

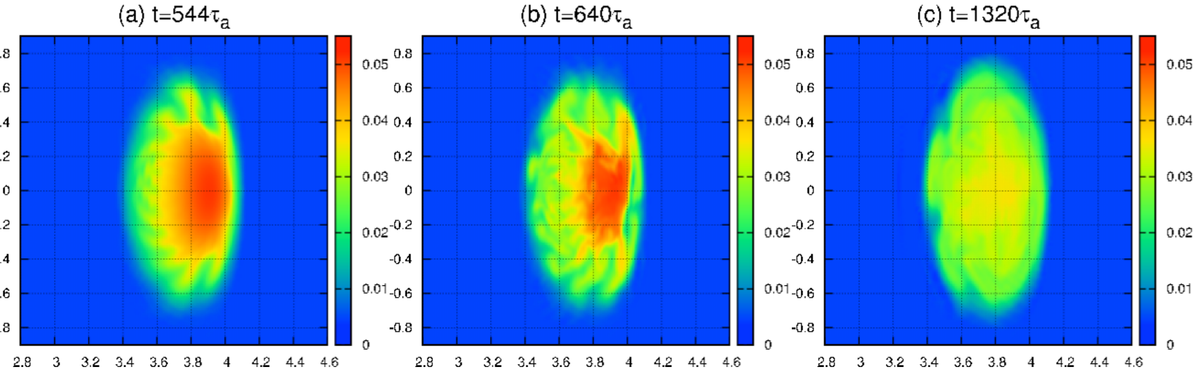

Fig.1. Time evolution of pressure profile on a poloidal section for $\beta_0$ =9.4% and S=$10^6$.

[1] Y. Todo. et al., Plasma Fusion Res. 5 (2010) S2062.

[2] Y. Suzuki et al., Nucl. Fusion 46 L19.

[3] N.Nakajima et al., Nucl. Fusion 46 (2006) 177.

[4] L. Chacón, Phys. Plasmas 15 (2008) 056103.

# 乱流計測シミュレータを用いた非拡散輸送過程の数値診断

## Numerical Diagnostics of Non-Diffusive Transport Process by Use of Turbulence Diagnostic Simulator

N. Kasuya, M. Sasaki, S. Inagaki, K. Itoh [1], M. Yagi [2] and S.-I. Itoh
Research Institute for Applied Mechanics, Kyushu University, Kasuga, Fukuoka 816-8580, Japan
[1] National Institute for Fusion Science, Toki, Gifu 509-5292, Japan
[2] Japan Atomic Energy Agency, Obuchi, Rokkasho-mura, Aomori 039-3212, Japan
E-mail: kasuya@riam.kyushu-u.ac.jp

A simulation of heat source modulation is carried out to understand plasma turbulent transport, including non-local responses. In this simulation, the pressure source term is modulated in the nonlinear saturation state of drift-interchange mode turbulence in helical plasmas. Characteristic response to the modulation can be extracted by the conditional averaging. It is found that the heat flux increases abruptly after the gradual change of the flux and pressure gradient on the onset of the additional heating, which is associated with variations of global modes propagating from core to edge. This process can cause immediate energy transfer to distant locations in magnetically confined plasmas.

Many experiments have revealed that local flux-gradient relation is insufficient to describe plasma dynamics in torus, and non-local effects should be taken into account to understand transient transport phenomena, e.g. L/H transitions. To clarify the transport dynamics, response to active control with additional modulation are studied. In ECH modulation experiment, conditional average shows sudden change of fluctuation amplitude in spite of gradual change of temperature, and hysteresis in the flux-gradient relation [1]. There is another experimental observation of global structures in torus plasmas [2], which is one of the candidates to cause immediate transfer to separated positions. Therefore, the role of the global structure on transport must be clarified.

Here, we carried out a global simulation of plasma turbulence with source modulation in torus, using Turbulence Diagnostic Simulator (TDS) [3]. The TDS is combination of fluid turbulence codes, measurement modules and analysis routines, to carry out numerical experiments of turbulent structural formation. In this study, drift-interchange modes in helical plasmas are analyzed using a reduced MHD model [3]. The pressure profile is sustained with the applied source, which has the peak at the plasma center. Simulations are performed with Fourier modes $-32 \leq m \leq 32$, $-8 \leq n \leq 8$, where $m$ and $n$ are the poloidal and toroidal mode number, respectively. Low $m$, $n$ modes are excited in the linear growing phase, and saturation is obtained with energy exchanges between various modes by nonlinear couplings. In the nonlinear saturated state, modes spreading broadly in the radial direction, such as $(m, n) = (1, 1)$ and $(2, 1)$, and localized near their rational surfaces, such as $(3, 2)$ and $(5, 5)$, are both excited. These fluctuations have the self-correlation time of 50 Alfvén time, though those of higher $m$ modes are smaller than 10 Alfvén time. The former and latter corresponds to the correlation times of the global modes and micro modes, respectively.

Response to additional modulation is investigated to clarify the nonlinear dynamics. The additional source is switched on and off cyclically. Characteristic response to the modulation is extracted by the conditional averaging over 100 cycles of the modulation. The additional source is only applied near the plasma center. Figure 1 shows the time evolutions of the pressure, its gradient and the heat flux at the position without the direct modulation to see how the pressure modulation propagates from the center. The additional source is switched on at $t = 0$ and off at $t = \pm 500$ in these figures. In this region, the pressure has time delay from $t = 0$, as the distance from the additional source region becomes larger. The heat flux increases as the pressure gradient increases, and vice versa. The heat flux also has the time delay, as shown in Fig. 1 (c), and it is accelerated from $t \sim 60$ to give the same rump-up rate at different radii. The transition between two states takes place in $t_{\mathrm{up}}$ ~200, which is much smaller than the characteristic time for pressure evolution ~ 500.

The mechanism of this response can be explained with the response of the global mode as $(m, n) = (2, 1)$ fluctuation (Fig. 2). The heat source modulation affects the global mode in $r / a < 0.3$, and the modulation propagates outward, as indicated by the additional line. This propagation corresponds to those in the pressure and the heat flux. Typical time scale for the propagation comes from the transit-time by the diamagnetic velocity ~ 100 Alfvén time, which is much smaller than that of the collisional diffusion ~ 1000 Alfvén time. The former and latter is the turbulence response time and the global confinement time, which is the two different time scales included in this simulation. The modulation can propagate rapidly in the region where the global mode spreads, which can be identified with the large radial correlation [4]. When the modulation reaches to the position at $r / a \sim 0.6$, acceleration of the ramp-up takes place. This is the region, where the nonlinear couplings cause the variation of the other modes. The profile modification arises in this region, and propagates to the other regions with the shorter time scale characterized by the self-correlation time of higher $m$ modes, which is smaller than 10 Alfvén time. In this way, rapid propagation of the heat modulation mediated by the global mode takes place. The dynamics of their radial profiles reveal the role of global mode on transport, and the mechanism of propagation to separated radial locations.

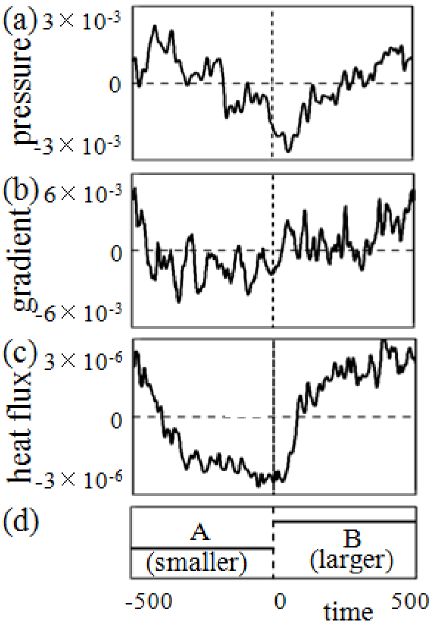

Fig. 1: Time evolutions of (a) the pressure, (b) absolute value of its gradient, (c) heat flux at $r / a = 0.6$ and (d) the source amplitude. The values are the deviations from the mean value at each radius.

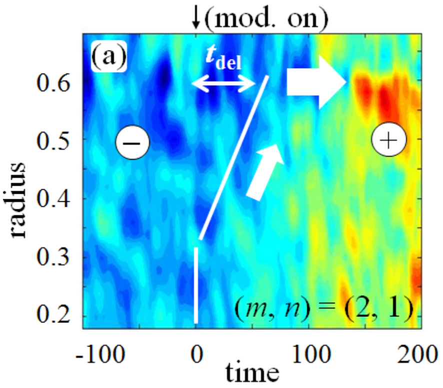

Fig. 2: Time evolutions of radial profiles of the global mode (2, 1). Deviation from the mean value at each radius is plotted.

[1] S. Inagaki, et al., Nucl. Fusion **53** (2013) 113006.
[2] S. Inagaki, et al., Phys. Rev. Lett. 107 (2011) 115001.
[3] N. Kasuya, et al., Plasma Fusion Res. 8 (2013) 2403070.
[4] N. Kasuya, et al., Plasma Fusion Res. 6 (2011) 1403002.

# Numerical simulations of structural formation in resistive drift wave turbulence

M. Sasaki[a,b*], N. Kasuya[a,b], K. Fukunaga[c], S. Inagaki[a,b], K. Itoh[b,d], M. Yagi[b,e], Y. Nagashima[a,b],
and S.-I. Itoh[a,b]

[a]*Research Institute for Applied Mechanics, Kyushu University,*
*Kasuga, Fukuoka 816-8580, Japan*
[b]*Itoh Research Center for Plasma Turbulence, Kyushu University,*
*Kasuga, Fukuoka 816-8580, Japan*
[c]*Interdisciplinary Graduate School of Engineering Sciences, Kyushu University,*
*Kasuga, Fukuoka 816-8580, Japan*
[d]*National Institute for Fusion Science, Toki, Gifu 509-5292, Japan*
[e]*Japan Atomic Energy Agency, Rokkasho, Kamikita, Aomori 039-3212, Japan*

* *Email: sasaki@riam.kyushu-u.ac.jp*

Importance of meso-scale structures such as zonal flows and streamers has been widely recognized for turbulent transport in improved confinement states of magnetized plasmas [1]. The elementary process for formation of the turbulent structures and their selection rule is considered in simple cylindrical geometry [2]. Recently, a macro-scale structure with a finite $m$, where $m$ is the azimuthal mode number, has been identified in experiments [3], and the nonlinear coupling with the turbulence has been confirmed [4]. A streamer [5] and flute type structure [6] are examples of the structures with finite $m$. These types of nonlinear structures directly induce radial transport due to their poloidal inhomogeneities, and have their own characteristic effects to determine the level of transport. In addition, there can be formed a solitary vortex [7] in a rather less unstable case. Thus, it is important to identify their role on transport; whether their formation enhances or suppresses the total transport [8]. In this view point, it is necessary to understand the fundamental processes and the competition among these nonlinear structures.

Simulation code Numerical Linear Device (NLD) is used, which is based on a three-field fluid model (density, potential and electron velocity parallel to the magnetic field) for the resistive drift wave turbulence in cylindrical magnetized plasmas [2]. A particle source term is introduced, and self-consistent nonlinear saturations of turbulence are obtained in three-dimensional turbulence simulations.

Selective formation of a zonal flow, streamer and flute structure is obtained by changing the strength of the particle source $S_0$, which corresponds to the driving force of the instability, as is shown in Fig. 1. Here, the definition of the energies of the flute structure, drift wave, mode with $n = 0$, and zonal flow

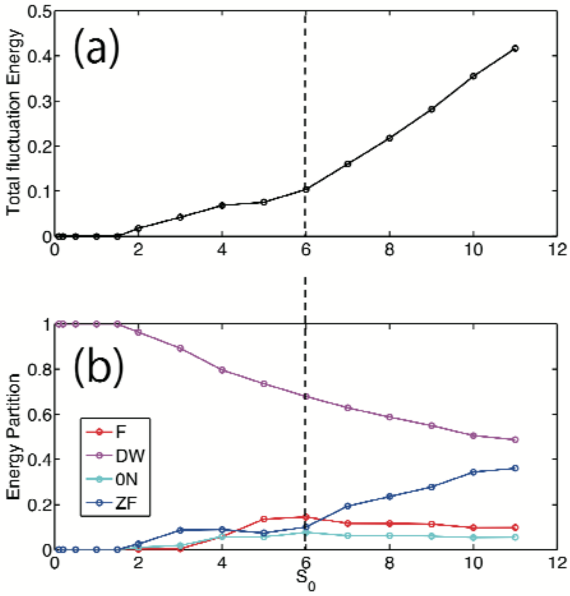

Fig.1. Source strength dependences of (a) the total fluctuation energy, and (b) energy partitions among the flute structure, drift wave, mode with $n = 0$, and zonal flow.

are in [9], where $n$ is the axial mode number. The streamer appears in the weak turbulent cases around $2 < S_0 < 4$. The flute structure, which is linearly stable, becomes dominant just below the marginal stability region of the zonal flow around $4 < S_0 < 6$. The turbulent structures which enhance the transport, such as the streamer and flute structure, are dominant in the smaller source cases. The energy partition of the zonal flow exceeds that of the flute structure around $S_0 = 6$, and the zonal flow is dominant in the larger source cases even with the existence of the flute structure.

The particle confinement properties in the turbulent states are investigated. The streamer and the flute structure enhance the transport, and affect the amplitudes of the drift waves and the zonal flow by nonlinear couplings. The dependence of the total particle number is shown in Fig. 2. The property of the confinement changes around $S_0 = 2$, where the drift wave is linearly destabilized, and around $S_0 = 6$, where the zonal flow begins to be effectively driven. In the cases with $S_0 < 2$, the drift wave is linearly stable, and the diffusion term determines the density profile, where the total particle number is proportional to the strength of the source. In the cases with $2 < S_0 < 6$, where the streamer or the flute structure is dominant, the total particle number follows the scaling as 0.72 power of the strength of the source strength. This scaling is similar to the L-mode plasma, where the energy confinement time follows 0.5 power of the strength of the input power [10]. In the cases with $S_0 > 6$, the total particle number increases in proportion to the strength of the source, so the particle confinement is improved. In this way, the spontaneous change in the transport property is obtained even in the cylindrical magnetized plasmas.

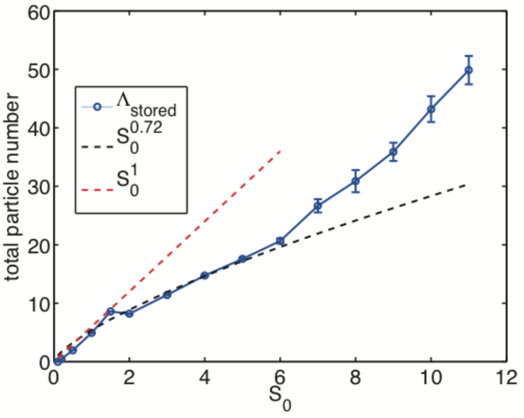

Fig.2. Source strength dependence of the total particle number.

The condition for formation of the solitary vortex is also studied. This structure is formed by nonlinear couplings of harmonics with a single dominant unstable mode [7]. Linear analyses show that a strong diffusion term and /or peaked density profile give the condition. Based on the results, nonlinear simulations are carried out to form the structure selectively with a steeper density gradient, which has convergence of waves at the wave front. The strength of the convergence corresponds to the strength of the localized radial transport, so is important to evaluate dynamics of the transport.

## References

[1] P. H. Diamond, et al., Plasma Phys. Control. Fusion **47**, R35 (2005).
[2] N. Kasuya, et al., Phys. Plasmas **15**, 052302 (2008).
[3] S. Inagaki, et al., Phys. Rev. Lett., **107**, 115001 (2011).
[4] T. Kobayashi, et al., Plasma Phys. Control. Fusion **54**, 115004 (2012).
[5] T. Yamada, et al., Nature Phys. **4**, 721 (2008).
[6] D. Biskamp, et al., Phys. Rev. Lett., **30**, 706 (1995).
[7] H. Arakawa, et al., Plasma Phys. Control. Fusion **51**, 085001 (2009).
[8] K. Itoh, et al., Plasma Phys. Control. Fusion, **54**, 115004 (2012).
[9] M. Sasaki, et al., submitted to Nucl. Fusion (2013).
[10] U. Stroth, et al., Nucl. Fusion, **35**, 131 (1995).

# Modeling of turbulence in the edge-core coupling region in tokamak plasmas

Y. Kosuga[1,2]

[1] Institute for Advanced Study, Kyushu University, Japan
[2] Research Institute for Applied Mechanics, Kyushu University, Japan

Predictive modelling of turbulent transport is essential to the success of ITER and DEMO. While numerical simulation has been succeeding in reproducing experimental observations, recent validation study identified the problem of short fall[1]. In that study, turbulent ion and electron heat flux was observed in L-mode plasmas and compared to the prediction from numerical simulations (TGLF, GYRO, GEM). The basic trend was that while both experiments and simulations agree in the core region, the disagreement becomes prominent toward the edge region. In particular, in the region that connects the core and the edge with $\rho = 0.6 \sim 0.8$, the predicted level is lower by roughly factor of 2 than the observed value. This is the problem of short fall. The short fall issue indicates that in order to model turbulence in the edge-core coupling region, new effects are required in addition to the conventional turbulence models assumed in the simulations.

An effect that is missed from the conventional modelling is the effect of non-locallity. There are several candidates that can contribute to the turbulence level in the coupling region non-locally, as shown in Fig.1.[2] Among these, here we focus on the incoming holes from the edge[2,3]. These holes are generated in the relaxation process associated with the steep gradient in the edge region. In this process, a pair of a hole and a blob is generated. Once generated, a blob propagates down the gradient while a hole propagates against the gradient and releases a free energy. Since propagating holes can enter the edge-core coupling region and release free energy stored in the region, holes are important element in understanding the phenomenology in the edge-core coupling region.

In modelling the dynamics of holes or blobs, an important variable is the potential vorticity(PV). For example, a basic model for describing drift wave turbulence, such as Hasegawa-Mima or Hasegawa-Wakatani model, conserves potential vorticity $dq/dt = 0$, where $q = (1 - \nabla_\perp^2)\phi$ for HM model or $q = n - \nabla_\perp^2\phi$ for HW model, $\phi$ is electrostatic potential and $n$ is density. PV conservation constraints the dynamics of porpagaing holes as shown in Fig.2. Due to the PV constraint, hole growth must involve acceleration of flows. Thus flow dynamics is important to understand self-consistent dynamics of propagating holes. The overall coupled dynamics determines the level of hole-induced transport, which can be a part of relaxation process in the edge-core coupling region.

Fruitful discussion with P.H. Diamond, O.D. Gurcan, G. Dif-Pradalier, S.-I. Itoh, K. Itoh, S. Inagaki, M. Lesur is acknowledgeged. This work was supported by Grants-in-Aid for Scientific Research of JSPF of Japan (21224014,25887041).

**References**: [1] T.L. Rhodes, et al.: Nucl. Fusion **51** (2011) 063022 [2] Y. Kosuga, et al.: Nucl. Fusion **53** (2013) 043008 [3] Y. Kosuga and P.H. Diamond: Plasma Fusion Res. **8** (2013) 2403080

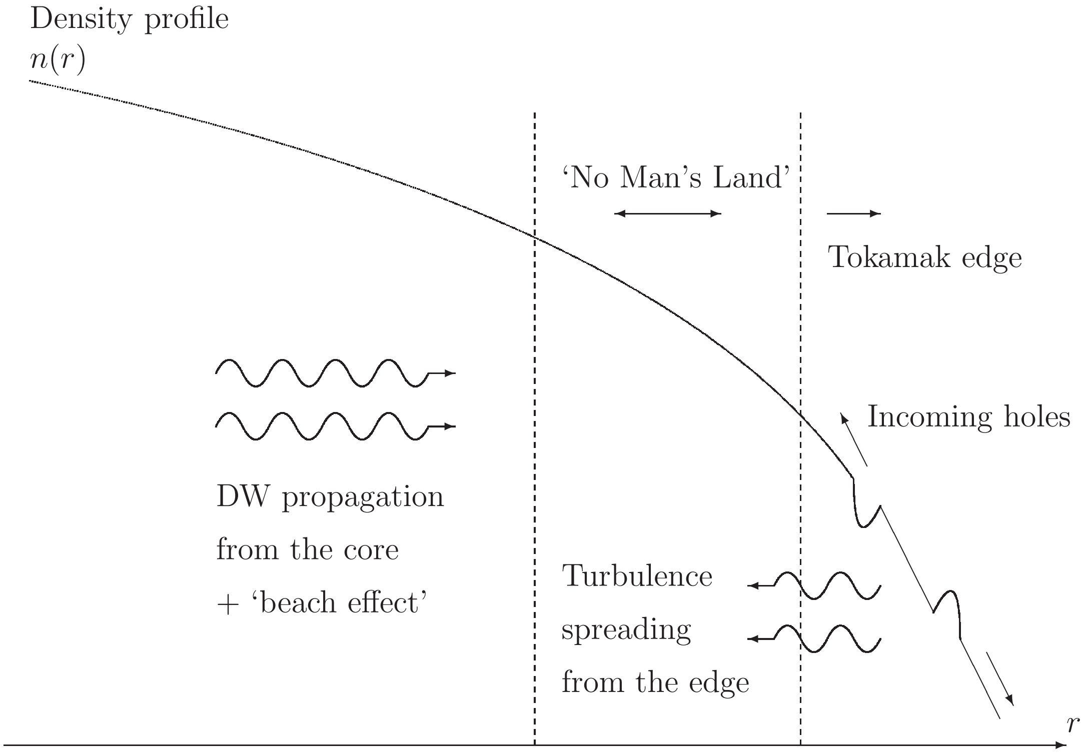

Figure 1: Several processes that can contribute to turbulence in the edge-core coupling region. These include, but not limited to, incoming holes from the edge, turbulence spreading from the edge, drift waves propagating from the core with beach effect. These processes can *non-locally* enhance turbulence level in the connecting region.

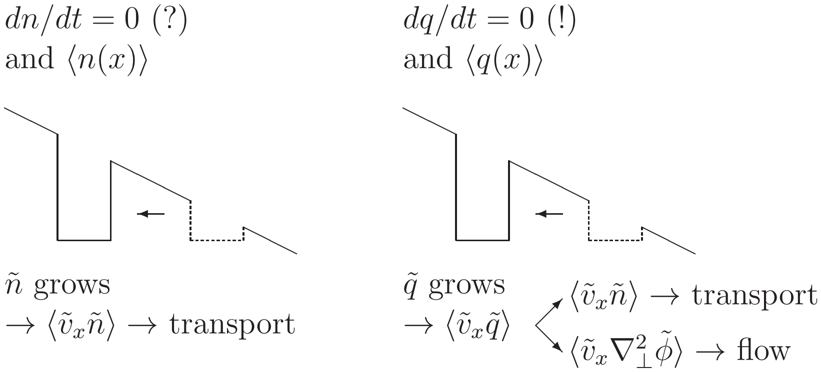

Figure 2: A cartoon for the contrast between $dn/dt = 0$ and $dq/dt = 0$. If $dn/dt = 0$, propagating holes grow by extracting free energy and cause transport. On the other hand, if $dq/dt = 0$, not only holes drive transport, but also they drive flows. The coupling between propagating holes and flows determine overall dynamics and transport level.

# Anomalous configuration of hydrogen trapped in tungsten vacancy and its application to plasma facing material

Kazuhito Ohsawa[1] and Yuuji Hatano[2]
[1]Research Institute for Applied Mechanics, Kyushu University
[2]Hydrogen Isotope Research Center, University of Toyama

## Introduction

Investigation of interaction between hydrogen (H) isotopes (D and T) and tungsten (W) is an important subject in the field of plasma facing materials (PFMs) because W and its alloys are promising as divertor armor tiles installed in future fusion reactors. We investigate stable configurations of H atoms trapped in bcc transition metals in terms of first-principle calculations. Anomalous H configurations are found associated with multiple H atoms trapped in a W vacancy. We estimate correct binding energy of each H isotope to the W vacancy on the basis of the valid H configurations. It is enabled us to study on isotope exchange mechanism and vacancy-hydrogen (V-H) cluster concentrations at finite temperature.

## Methodology

First-principle calculations are performed using Vienna ab initio simulation package (VASP) based on density functional theory. Binding energy, $e_k$, of H or H isotopes to a W vacancy is defined, as follows.

$$e_k = \mathrm{E}[\mathrm{W}_{n-1}\mathrm{V}] - \mathrm{E}[\mathrm{W}_{n-1}\mathrm{VH}_k] - k(\mathrm{E}[\mathrm{W}_n\mathrm{H}^{\mathrm{T}}] - \mathrm{E}[\mathrm{W}_n]),$$

where the function E is the cohesive energy of the supercell. For example, $\mathrm{W}_{n-1}\mathrm{VH}_k$ indicates a supercell composed of $n$-1 W, a vacancy V, and $k$ H atoms. V-H cluster concentrations at finite temperature are calculated in an equilibrium thermodynamic model.

## Stable configuration of H atoms

Tetrahedral and octahedral sites (T site and O site) are typical interstitial positions in bcc lattice, as shown in Fig. 1 (a). It has been reported that an H atom prefers to be located at T site in bcc transition metals. While, a single H atom trapped in a vacancy is located on the inner surface of the vacancy close to an O site, as shown in Fig. 1 (b).

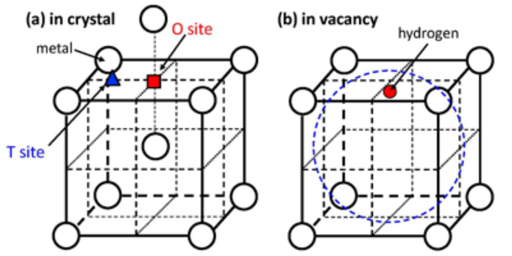

Fig. 1: (a) Typical interstitial sites, T site and O site, in BCC metals. (b) Stable position of single H trapped in vacancy close to O site.

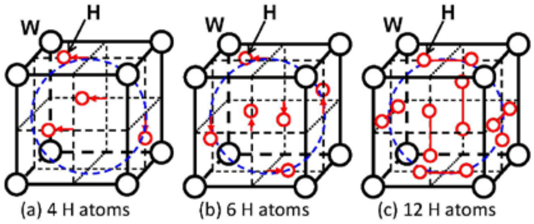

Fig.2: Stable configurations of multiple H atoms in W vacancy. Characteristic configurations of 4, 6, 12H atoms in W vacancy.

A maximum of 6 H atoms is believed to be trapped in a vacancy in bcc transition metals because there are 6 O sites next to the vacancy. However, H atoms in a W vacancy are shifted in the <100> directions from the O sites, as the number of H atoms in the vacancy increases. Figure 2 shows some characteristic stable configurations of multiple H atoms in the W vacancy. (a) Stable configuration of 4 H atoms is tetrahedral structure but planar one. (b) Stable configuration of 6 H atoms is complicated. 4 H atoms out of the 6 are displaced from O sites by about 18 % of the lattice constant in the <100> directions, and the remainder of the H atoms are slightly shifted from O sites. (c) 12 H atoms in a W vacancy are located close to T sites.

It has been reported that a vacancy in usual bcc transition metals is capable of accommodating 6 H atoms. However, a maximum of 12 H atoms can be accommodated in a W vacancy.

**Application to study on plasma facing material**

Tritium absorption and desorption are an important subject for PFMs in fusion reactors because T is a radioisotope whose half-life is 12 years. Isotope exchange is expected to be an effective method to induce T desorption from the PFMs. The binding energy of T to a W vacancy is supposed to be smaller than that of other H isotopes. The isotope exchange is caused by the energy difference. It is necessary to calculate correct zero-point vibrational energies on the basis of the valid H configurations. We estimate binding energies of H and T to a W vacancy and confirm the expectation, as shown in Fig. 3.

V-H cluster concentrations are calculated in an equilibrium thermodynamic model at finite temperature and H concentration in a bulk W. A maximum of 12 H atoms can be accommodated in a W vacancy at 0K, according to first-principle simulations. However, the major V-H clusters are composed of 6 H atoms in a wide range of temperature and H concentration. Figure 4 is an example of V-H cluster distribution.

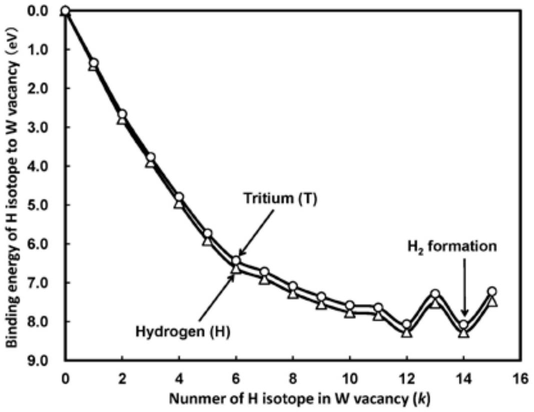

Fig3: Binding energy of H and T to W vacancy as a function of the number of H atoms trapped in W vacancy.

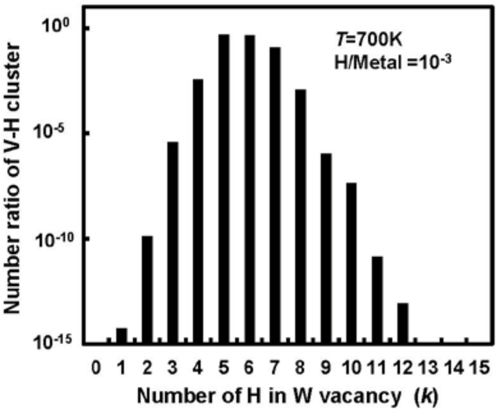

Fig. 4: Number ratio of V-H cluster distribution at H concentration $10^{-3}$ and *T*=700K.

# Particle Simulation of Peripheral Plasmas in Tokamaks using PARASOL

[1]**Shuhei AZUMA**, [1]**Atsushi FUKUYAMA, and** [2]**Tomonori TAKIZUKA**
[1]Graduate School of Engineering, Kyoto University
[2]Graduate School of Engineering, Osaka University

## 1 Introduction

In tokamak reactors, peripheral plasma is expected to play an important role as an acceptor of high heat flux and particles, such as fuel, helium ash, and impurities, from core plasma. The flow in peripheral plasmsa is also expected to take them to the divertor, where they are removed [1]. Their permformance have been so far examined by fluid simulations, while these simulations couldn't give a satisfactory exlanation for some results of experiments conducted to investigate the flow [2].

On the other hand, recent studies have demostrated, based on particle simulations using PARASOL, that the effects of finite-orbit-size of ions are essential for the formation of the plasma flow [3], and have developed a new model of the flow, called "ion-orbit-induced flow", for comprehensive divertor simulation with fluid models [4]. Since the simulations for the previous studies did not take into account recycling or radiation cooling, however, little is still known about their effects on the peripheral plasma flow.

We examined in this study, by using full particle simulation code PARASOL, how recycling in the vicinity of the divertor affects peripheral plasma flow. Also note that we do not consider here radiation cooling in order to focus on the effect of recycling.

## 2 PARASOL simulation models

The two demensional PARASOL (PARASOL2D) is a full particle simulation code which simulates a scrape-off layer (SOL) and divertor plasma in the toroidal system with cylindrical coordinates, employing the particle-in-cell (PIC) method, along with a binary collision model [3]. The spatial configuraion is shown in Fig. 1. It should be noted that adjusting the ratio of upper- and lower-divertor coil currents make two divertor configurations possible; an upper null (UN) and lower null (LN) configuration.

We consider that plasma consists of electrons and single-species ions, and any ion is assumed to be charged singly for simplicity. The motion of electrons is approximated by their guiding-center motion, while that of ions is fully followed. The electric field is calculated self-consistently with the PIC method, on the assumption that boundary walls surrounding plasma are electrically conductive. Anomalous transport is simulated with a Monte-Carlo random-walk model, and the effect of Coulomb collisions is added by a binary collision model.

A particle is assume to be absorbed when reaching divertor plates, and to be reflected when arriving at the other side walls. Given that $\Delta N_{\mathrm{loss}}$ is the number of lost ions in one time step, in the following time step, $(1 - R)\Delta N_{\mathrm{loss}}$ pairs of an electron and an ion are supplied in the central region H, and the $R\Delta N_{\mathrm{loss}}$ pairs in the recycling area C1 and C2, at a prescribed temperature (see Fig. 1 for H, C1, and C2). Here $R$ represents a recycling rate and have the values of 0, 0.5, 0.7, 0.8, and 0.9 in this study. As for other paramters, the number of simulation ions $N_i$ is $10^6$ and the number of spatial cells $M_R \times M_Z$ is $320 \times 512$. The pitch of the magnetic field $\Theta$ is 0.2, and the aspect ratio is set as $A = 5.5$. The mass ratio $m_i/m_e$ is 1800, The normalized ion Larmor radius $\rho_i/a \sim 0.02$, the collisionality $L_\parallel/l_{\mathrm{mfp}} \sim 1$, and the normalized diffusion coefficient $D_{\mathrm{anom}}/aC_s \sim 10^{-5}$ ($C_s$ is a sound speed).

## 3 Results

Figure 2 shows, for the values of recycling rates, simulation results of the patterns of the SOL flow parallel to the magnetic field in the cases of (a) the LN and (b) the UN configuration, where the direction of ion $\nabla B$ drift is downward. In the figure, red expresses the co-flow to the plasma current, while blue refers to the counter-flow. The red co-flow and blue counter flow represent anti-clockwise and clockwise flow in the poloidal cross-section. It has proved evident from these results that recycling has little impact on SOL plasma flow patterns.

We also examined the ion Mach number parallel to the field at the divertor throat near the X point, $M_{\rm th}$, to gain a quantitive understanding of the recycling effect on the flow. Considering $M_{\rm th} = |V_i|/C_{\rm s}$ ($C_{\rm s} \equiv \sqrt{T/m_i}$), and using $V_i$ and $T$ from simulation results, we can obtain $M_{\rm th}$ (called measured $M_{\rm th}$ for convinience here ). On the other hand in the study of the one dimensinal SOL plasma system, it have been verified that $M_{\rm th}$ can be approximated by using the relation, $M_{\rm th} \sim \sqrt{T_{\rm p}/T_{\rm th}}/2F_\Gamma$, in the case of high recycling rates [5]. (Also it is conventionally called calculated $M_{\rm th}$ here.) We note here that $F_\Gamma = 1/(1-R)$, and the index $p$ denotes a quantity measured in front of diverter plates. Figure. 3 shows the comparison of measured $M_{\rm th}$ with calculated $M_{\rm th}$ by $F_\Gamma$. It follows from these data that $M_{\rm th}$ is less subject to the recycling effect in the 2D toroidal system where the ion-orbit-induced flow dominates.

## References

[1] A. Loarte *et al,* Progress in the ITER Physics Basis Chapter4:Power and particle control *Nucl. Fusion* **47** S203 (2007)

[2] N.Asakura and ITPA SOL and Divertor Topical Group, *J. Nucl. Mater.* **363-365** 41 (2007)

[3] T. Takizuka, K. Shimizu, N. Hayashi, M. Hosokawa, and M. Yagi, *Nucl. Fusion* **49** 075038 (2009)

[4] T. Takizuka, K. Hoshino K. Shimizu, and M. Yagi, *Contrib. Plasma Phys.* **50** No.3-5, 267—272 (2010)

[5] T. Takizuka, M. Hosokawa, K. Shimizu, *J. Nucl. Mater.* **753** (2001) 290-293

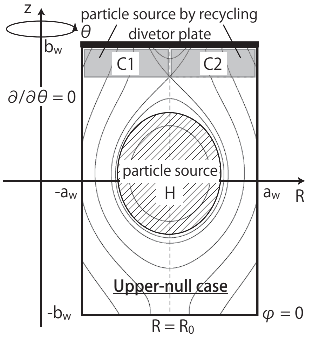

Figure 1: Space configuration for the upper null case

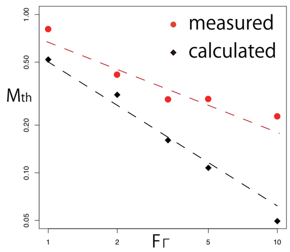

Figure 3: $F_\Gamma$ vs. measured and calculated $M_{\rm th}$

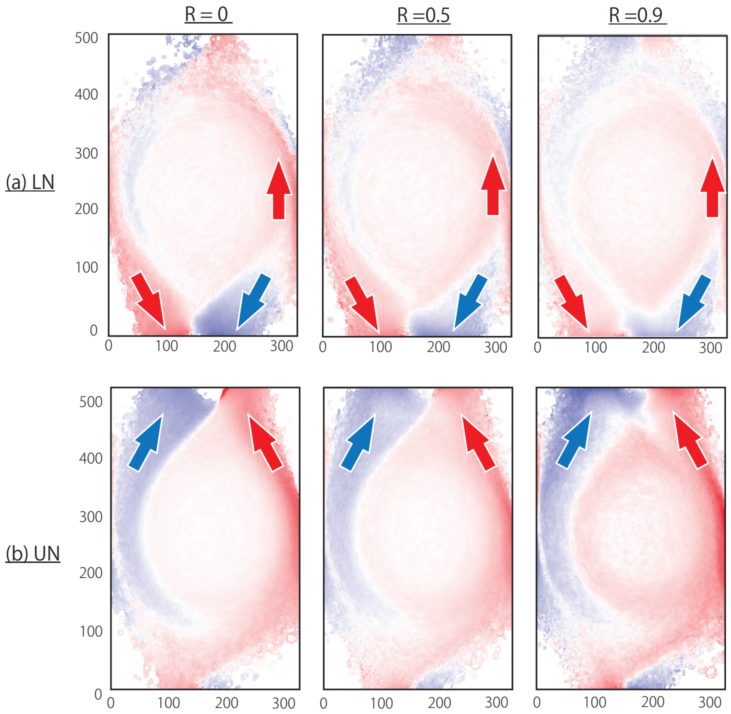

Figure 2: Simulation results of plasma flow patterns

# Progress of ITER Integrated Modeling Activity

A. Fukuyama

Department of Nuclear Engineering, Kyoto University, Kyoto, Japan

For the success of the ITER project, the role of integrated modeling of burning plasmas is essential. It is necessary for operation support (preparation, execution, reconstruction) and plasma research (model validation, scenario development, upgrade of equipments). The modeling activity is a part of activities in Science Division of Plasma Operation Department of ITER organization. In order to promote collaboration with ITER participating parties, the Integrated Modelling Expert Group (IMEG) takes the role of adviser for the development of integrated modelling codes and topical groups of International Tokamak Physics Activity (ITPA) contribute construction of experimental database, development and validation of physics models, and operation scenario development.

The present main activity of ITER integrated modeling is to complete the conceptual design of Integrated Modelling Analysis Suite (IMAS). The conceptual design has been carried out by a contract with a research group from EU. IMAS will be constructed based on a common infrastructure and various components implementing physics models are combined with each other for specific purpose. The components will be developed mainly by participating parties conforming with the ITER Modelling standard.

The infrastructure includes

- Physics data model (Data structure, Data specification)
- Component model (Application program interface)
- Workflow tool (Compilation of components, data flow)
- Monitoring (Real time data glancing)
- Life cycle (How to upgrade data models)

For physics data mode, rules and guidelines have been documented and a preliminary set of Interface Data Structure (IDS) are available. Table 1 indicates the list of IDS in Physics Data Model v2.0. Each IDS includes various data. As an example, the data definition of IDS core profile is shown in Table 2. The structure data ids_properties is

Table 1 List of IDS in v2.0

| IDS name | Description |
|---|---|
| actuator | Generic simple description of a heating/current drive actuator |
| controllers | Feedback and feedforward controllers |
| core profiles | Core plasma radial profiles |
| core sources | Core plasma source terms (for the transport equations) |
| core transport | Core plasma transport |
| em coupling | Description of the axisymmetric mutual electromagnetics |
| equilibrium | Description of a 2D, axi-symmetric, tokamak equilibrium |
| magnetics | Magnetic diagnostics for equilibrium identification and plasma shape control |
| pf_active | Description of the axisymmetric active poloidal field (PF) coils and supplies |
| pf_passive | Description of the axisymmetric passive conductors, currents flowing in them |
| schedule | Description of Pulse Schedule |
| sdn | Description of the Synchronous Data Network parameters and the signals on it |
| simulation | Simulation parameters for a general simulation |
| temporary | Storage of undeclared data model components |
| tf | Toroidal field coils (all assumed to be identical) |

a common data for all IDS. Since the data includes the time history, most of data is FLT_2D, two-dimensional floating data with radial and time index. The component model is similar to the interface of BPSD. As a workflow tool, KEPLER workflow engine is used and the transport code CORSICA was implemented on it. The procedure to update the infrastructure, especially the date model, is under discussion.

As an BPSI activity, the interface between BPSI (data model and application interface) and the ITER physics data model will be developed. The collaboration of the integrated codes in Japan, TOPICS, TASK, TASK3D, and TOTAL, will be promoted, and future contributions to IMAS should be discussed.

Table 2 Definition of IDS core profiles

| Full path name | Description | Data type |
|---|---|---|
| ids_properties | Interface Data Structure properties | structure |
| rho_tor_norm | Normalised toroidal flux coordinate | FLT_1D |
| vacuum_toroidal_field | Characteristics of the vacuum toroidal field | structure |
| psi | Poloidal magnetic flux | FLT_2D |
| t_e | Electron temperature | FLT_2D |
| t_i_average | Ion temperature | FLT_2D |
| n_e | Electron density (thermal+non-thermal) | FLT_2D |
| n_e_fast | Density of fast (non-thermal) electrons | FLT_2D |
| ions | Quantities related to the different ion species | structure |
| ions/a | Mass of atom | FLT_0D |
| ions/z_ion | Ion charge | FLT_0D |
| ions/z_n | Nuclear charge | FLT_0D |
| ions/label | String identifying ion | STR_0D |
| ions/n_i | Ion density (thermal+non-thermal) | FLT_2D |
| ions/n_i_fast | Density of fast (non-thermal) ions | FLT_2D |
| ions/t_i | Ion temperature | FLT_2D |
| ions/p_i | Ion pressure | FLT_2D |
| ions/v_tor_i | Toroidal velocity | FLT_2D |
| ions/v_pol_i | Poloidal velocity | FLT_2D |
| ions/charge_states | Quantities related to the different charge states | structure |
| n_i_total_over_n_e | Ratio of total ion density over electron density | FLT_2D |
| momentum_tor | Total plasma toroidal momentum | FLT_2D |
| zeff | Effective charge | FLT_2D |
| p_e | Electron pressure | FLT_2D |
| p_i_total | Total ion pressure | FLT_2D |
| pressure_thermal | Thermal pressure (electrons+ions) | FLT_2D |
| pressure_perpendicular | Total perpendicular pressure | FLT_2D |
| pressure_parallel | Total parallel pressure | FLT_2D |
| j_total | Total parallel current density | FLT_2D |
| j_tor | Total toroidal current density | FLT_2D |
| j_ohmic | Ohmic parallel current density | FLT_2D |
| j_non_inductive | Non-inductive (includes bootstrap) parallel current density | FLT_2D |
| j_bootstrap | Bootstrap parallel current density | FLT_2D |
| conductivity_parallel | Parallel conductivity | FLT_2D |
| e_field_parallel | Parallel electric field | FLT_2D |
| q | Safety factor | FLT_2D |
| magnetic_shear | Magnetic shear | FLT_2D |
| global_quantities | Various global quantities derived from the Core_Profiles | structure |
| code | Generic description of the code specific parameters | structure |

# Progress of integrated transport analysis suite, TASK3D-a (analysis version), and its extensive application to LHD experiment

M.Yokoyama, R.Seki, C.Suzuki, S.Satake, M. Osakabe, K.Ida, S. Murakami*, H.Yamaguchi*, A.Fukuyama*, and LHD Experiment Group

National Institute for Fusion Science, 322-6, Oroshi-cho, Toki-city, 509-5292, Japan
*Department of Nuclear Engineering, Kyoto University, Kyoto 615-8540, Japan

The Large Helical Device (LHD) has steadily extended its parameter regime [1]. More importantly, not only the parameter extension, but also the increased diagnostic capability has provided a wide-range database to be exploited for the accurate physics discussion. Integrated transport analysis suite, TASK3D-a (Analysis version) [2], has been developed for conducting automated energy confinement analyses for NBI-heated plasmas in LHD. The capability of TASK3D-a has been gradually increasing. In this abstract, significance and usefulness of TASK3D-a are described from the viewpoints of its close link to LHD experiment data and then making systematic analyses possible.

Calculation flow of TASK3D-a consists of the three-dimensional equilibrium specification, NBI deposition and energy balance calculations, so that they are sequentially executed in an automated manner. It has an LHD experiment data interface part, which has a direct link to a so called LHD Kaiseki Data Server [3] and TSMAP (real-time coordinate mapping system) [4]. Processed diagnostics data are registered onto the Kaiseki Data Server in a common format (ASCII file, so called eg-format), and then mapping of profile data such as temperature and density (which are required for transport analyses) from the real geometry to the effective minor radius, $r_{eff}$, defined by TSMAP. Then mapped profile data are transferred to TASK3D-a as inputs. Some of TASK3D-a results (NBI deposition profile, ion and electron heat diffusivity etc.) are then registered to the Kaiseki Data Server for common use. Users just need to login to the Kaiseki Data Server for utilizing these results. The dataflow described above is conceptually drawn in Fig.1. The words written with small characters are names of registered data (so called eg data). The logo near the "TASK3D-a" is newly introduced logo for TASK3D collaborative research.

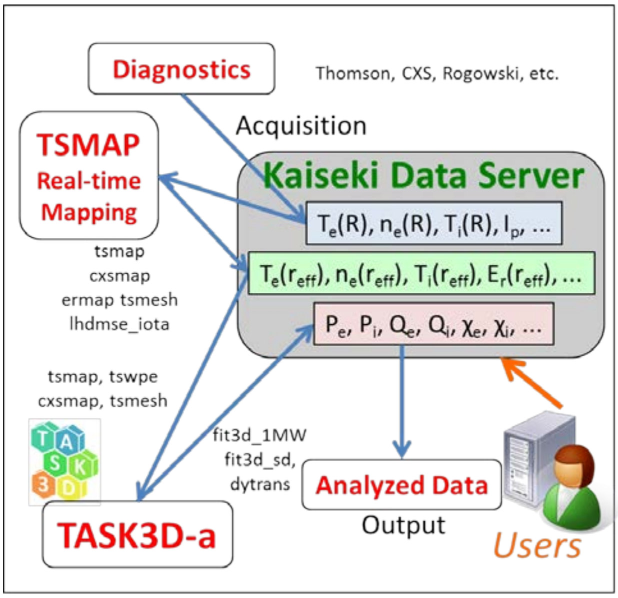

Fig.1 The close link between TASK3D-a (logo is attached) and LHD experiment data (centralized to LHD Kaiseki Data Server) is schematically shown.

In such a way, TASK3D-a, fully integrated into LHD experiment database, has smoothly utilized experimental data for increasing cases of analyses. So far, high ion temperature (Ti) plasmas [5] (Ti~5-7 keV, Ti>Te at the core with the density of $1\sim2\times10^{19}$ $m^{-3}$) and medium-to-high density plasmas [6] (Ti~Te~3-4 keV at the core with the density of $3\sim5\times10^{19}$ $m^{-3}$) have been extensively analysed. High-Te plasmas will also be analysed once ECH modules are fully integrated into TASK3D-a. So far, the order of $10^4$

timings has been analysed from multiple shots, including cases without Ti profile measurement (only Te and ne are available).

Figure 2, as an example of a systematic plot, shows the ion and electron heat diffusivity as a function of temperature ratio, Te/Ti, for $r_{eff}/a_{99}$~0.4 based on dynamic transport analyses. Here $a_{99}$ is the plasma minor radius in which 99 % of the total stored energy is confined. Generally, data for Te/Ti <1 correspond to high-Ti plasmas, and those for Te/Ti>1 to medium-to-high density plasmas. The diffusivity is normalized by Gyro-Bohm temperature scaling, $T^{1.5}$. The tendency is recognized that the normalized ion (electron) heat diffusivity increases (decreases) as Te/Ti is increased. It can be considered that high-Ti plasmas in LHD are situated in a Te/Ti regime with smaller ion diffusivity. From this systematic plot, it is implied that plasmas with Te~Ti are favourable from the viewpoint of simultaneously small ion and electron heat diffusivity. This implication is consistent with recent trials for increasing Te in high-Ti plasmas in LHD (from Ti>Te towards Ti~Te) through the increase of available ECH power.

The important feature of a huge TASK3D-a analysis database is that it stores plasma parameters, experimental power balance, neoclassical diffusion and dimensionless parameters etc., all in “PROFILES”. Thus, probably based on the statistical approach, it is anticipated to deduce **heat diffusivity scaling with radial dependence**, also distinguishing ion and electron channel. This will be one of research targets in the near future and will be reported in a separate opportunity. It should be far beyond the global energy confinement scaling [7,8], and thus significant increase of the predictive capability is expected. Such deduced scaling will be implemented into TASK3D-p, the predictive version of TASK3D.

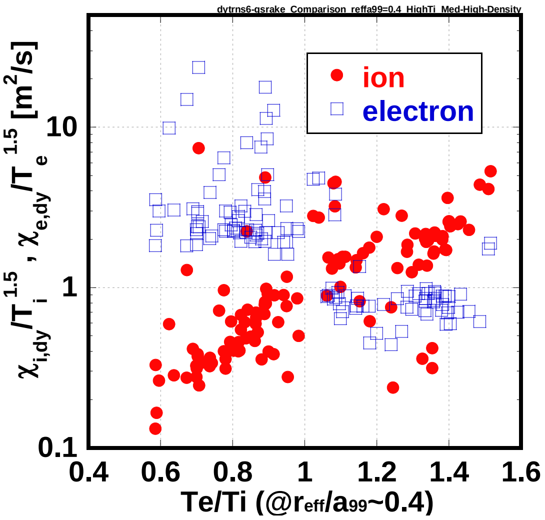

Fig.2 Example figures describing systematic dependence based on TASK3D-a analysis database (multiple shot-timings). Ion and electron heat diffusivity evaluated with the dynamic transport as a function of temperature ratio, Te/Ti at a specific radius ($r_{eff}/a_{99}$~0.4).

## Acknowledgements

The authors are grateful to LHD experiment group for making the experimental data available. This work has been supported by the NIFS Collaborative Research Programs, NIFS11KNTT008 and NIFS11UNTT006. One of authors (M.Y.) appreciates a grant-in-aid from the Future Energy Research Association.

## References

[1] O.Kaneko, H.Yamada et al., Nuclear Fusion 53 (2013) 104015.
[2] M.Yokoyama et al., Plasma and Fusion Res. 8 (2013) 2403016.
[3] M. Emoto et al., Fusion Eng. Des. 81 (2006) 2019.
[4] C.Suzuki et al., Plasma Phys. Control. Fusion 55 (2013) 014016.
[5] K.Nagaoka et al., Nucl. Fusion 51 (2011) 083022.
[6] A.Dinklage, M.Yokoyama et al., Nucl. Fusion 53 (2013) 063022.
[7] For example, ITER Physics Basis, Nucl. Fusion 39 (1999) 2175.
[8] H.Yamada et al., Nucl. Fusion 45 (2005) 1684.

# Particle transport simulation in tokamak plasma by TASK/TX

KANAMORI Ryosuke, FUKUYAMA Atsushi
Graduate School of Engineering, Kyoto Univ.

In a magnetic confinement nuclear fusion reactor, fusion output power is strongly influenced by fuel ion density. The density profile of fuel ions is govered by ionization and transport though the particle transport in tokamak plasmas is not yet well-known. In previous particle transport analyze, diffusion equation of particle flux has been solved for only ion particle transport and electron density is obtained by quasi-neutrality condition. In this report, we simulate particle transport by the TASK/TX code and try to resolve various issues in particle transport. TASK/TX is a 1D dynamic transport simulation code based on two-fluid equations. It solves particle transport of electron and ion simultaneously, and solves Gauss's law without using quasi-neutrality condition. It is able to describe the time evolution of density, rotation and temperature for each species. Our goal is to construct particle transport modeling which agrees with experimental observations by improving physics models and various parameter.

The set of 1D two-fluid equations is composed of equation of continuity for density $n_s$, equations of motion for radial velocity $u_{sr}$, poloidal and toroidal rotation $u_{s\theta}$, $u_{s\phi}$, and heat transport equation for internal energy $\frac{3}{2}n_sT_s$ and written as

$$
\begin{aligned}
\frac{\partial n_s}{\partial t} &= -\frac{1}{r}\frac{\partial}{\partial r}(rn_su_{sr}) + \frac{1}{r}\frac{\partial}{\partial r}\left(rD_\mathrm{m}v_{Ts}\frac{\partial n_s}{\partial r}\right) + S_s \\
\frac{\partial}{\partial t}(m_sn_su_{sr}) &= -\frac{1}{r}\frac{\partial}{\partial r}(rm_sn_su_{sr}^2) + \frac{1}{r}rm_sn_su_{s\theta}^2 - \frac{\partial}{\partial r}(n_sT_s) + e_sn_s(E_r + u_{s\theta}B_\phi - u_{s\phi}B_\theta) \\
\frac{\partial}{\partial t}(m_sn_su_{s\theta}) &= -\frac{1}{r^2}\frac{\partial}{\partial r}(r^2m_sn_su_{sr}u_{s\theta}) + \frac{1}{r^2}\frac{\partial}{\partial r}\left[r^3m_sn_s\mu_s\frac{\partial}{\partial r}\left(\frac{u_{s\theta}}{r}\right)\right] + e_sn_s(E_\theta - u_{sr}B_\phi) \\
&\quad + \frac{1}{r}\frac{\partial}{\partial r}\left[rD_\mathrm{m}v_{Ts}\frac{\partial}{\partial r}(m_sn_su_{s\theta})\right] + F_{s\theta}^\mathrm{NC} + F_{s\theta}^\mathrm{C} + F_{s\theta}^\mathrm{W} + F_{s\theta}^\mathrm{L} + F_{s\theta}^\mathrm{N} + F_{s\theta}^\mathrm{CX} \\
\frac{\partial}{\partial t}(m_sn_su_{s\phi}) &= -\frac{1}{r}\frac{\partial}{\partial r}(rm_sn_su_{sr}u_{s\phi}) + \frac{1}{r}\frac{\partial}{\partial r}\left(rm_sn_s\mu_s\frac{\partial u_{s\phi}}{\partial r}\right) + e_sn_s(E_\theta + u_{sr}B_\theta) \\
&\quad + \frac{1}{r}\frac{\partial}{\partial r}\left[rD_\mathrm{m}v_{Ts}\frac{\partial}{\partial r}(m_sn_su_{s\phi})\right] + F_{s\phi}^\mathrm{C} + F_{s\phi}^\mathrm{W} + F_{s\phi}^\mathrm{L} + F_{s\phi}^\mathrm{N} + F_{s\phi}^\mathrm{CX} \\
\frac{\partial}{\partial t}\left(\frac{3}{2}n_sT_s\right) &= -\frac{1}{r}\frac{\partial}{\partial r}\left(\frac{5}{2}ru_{sr}n_sT_s - \frac{3}{2}rn_s\chi_s\frac{\partial T_s}{\partial r}\right) + e_sn_s(E_\theta u_{s\theta} + E_\phi u_{s\phi}) \\
&\quad + \frac{1}{r}\frac{\partial}{\partial r}\left[rD_\mathrm{m}v_{Ts}\frac{\partial}{\partial r}(n_sT_s)\right] + P_s^\mathrm{C} + P_s^\mathrm{L} + P_s^\mathrm{R} + P_s^\mathrm{RF}
\end{aligned}
$$

where terms including $D_\mathrm{m}$ represent diffusive effects due to magnetic surface destruction. The perpendicular viscosity $\mu_s$ and thermal conductivity $\chi_s$ represent anomalous transport due to the turbulence. The particle source $S_s$, neoclassical viscous force $F_s^\mathrm{NC}$, classical collisional momoentum transfer $F_s^\mathrm{C}$, forces due to the interaction with turbulence electric field $F_s^\mathrm{W}$, parallel transport loss in the SOL region $F_s^\mathrm{L}$, friction force with neutrals $F_s^\mathrm{N}$, charge-exchange force $F_s^\mathrm{CX}$, collisional energy transfer power $P_s^\mathrm{C}$, collisional energy loss power $P_s^\mathrm{L}$ bremsstrahlung power $P_s^\mathrm{R}$, and direct RF heating power $P_s^\mathrm{RF}$ are calculated from local quntities.

In the SOL region, $a < r < b$, where $a$ is the plasma radius and $b$ is the wall radius, losses along with magnetic field line is dominant. The loss rate of particle and ion heat are given by

$\nu_\mathrm{L} = C_s/L$ where $C_s$ is the sound speed and $L$ is the length of magnetic field line. Electron heat loss is modeled by collisional heat conductivity

$$\nu_{\mathrm{L}T_\mathrm{e}} = \frac{\kappa_0 T_\mathrm{e}^{5/2}}{L^2 n_\mathrm{e}} \quad \text{where} \quad \kappa_0 = \frac{(4\pi\epsilon_0)^2}{m_\mathrm{e}^{1/2} Z_\mathrm{eff} e^4 \ln \Lambda_\mathrm{e}}$$

When the electron heat loss flux rate exceeds the electron thermal velocity, the heat limiting model $\nu_\mathrm{Llim} = v_{T_\mathrm{e}}/L$ is introduced to give

$$\hat{\nu}_{\mathrm{L}T_\mathrm{e}} = \frac{\nu_{\mathrm{L}T_\mathrm{e}} \cdot \nu_\mathrm{Llim}}{\nu_{\mathrm{L}T_\mathrm{e}} + \nu_\mathrm{Llim}}$$

Magnetic surface destruction by magnetic perturbation in plasma edge region causes particle and heat diffusion. In the case of low collisionality, the radial diffusion coefficient $D_s$ is proportional to the thermal velocity $v_{Ts}$.

$$D_s \equiv \frac{\left\langle (\Delta r)^2 \right\rangle}{\tau} = \begin{cases} D_\mathrm{m} v_{Ts} & (r_\mathrm{min} < r < r_\mathrm{max}) \\ 0 & (\text{otherwise}) \end{cases}$$

where the magnetic diffusion rate in length $\lambda$ is given by

$$D_\mathrm{m} \equiv \frac{\left\langle (\Delta r)^2 \right\rangle}{\lambda}$$

First, we analyse the influence of heat limiting model. The dashed curve is the result with heat limiting model, and the solid one is classical model in Fig.1. With the heat limiting model, abrupt change of electron temperature at the plasma edge disappears.

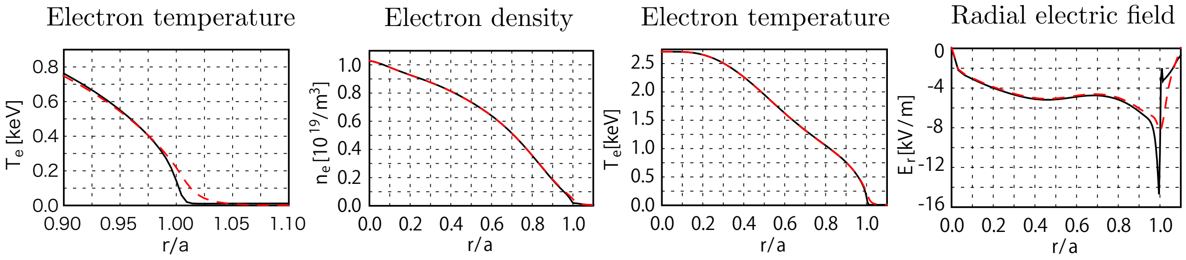

Fig.1

Next, we analyze effect the of magnetic surface destruction. The solid curve in Fig.2 is the case without destruction, and the dashed one is the case with $D_\mathrm{m} = 7.0 \times 10^{-10}\,\mathrm{m}^{-1}$ for $0.85 < r/a < 1.05$. The radial electric field changes strongly though there is little change in the density profile.

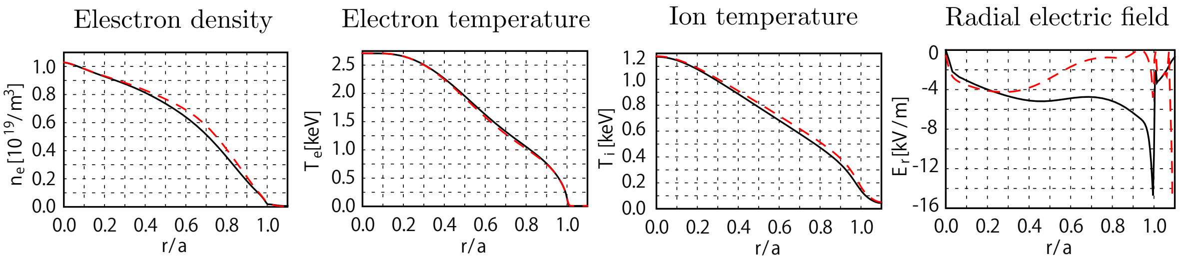

Fig.2

We have examined some parameter dependences in particle transport simulation by TASK/TX to improve the agreement with experimental observations. Electron temperature becomes smooth at the plasma edge by using the heat limiting model. More improvement of the modeling is required to describe the effect of magnetic surface destruction.

# DIII-D におけるアルフベン固有モードと高速イオン輸送のシミュレーション
# Simulation of Alfvén eigenmodes and fast ion transport in DIII-D experiment

Y. Todo[1)], M. A. Van Zeeland[2)], A. Bierwage[3)], W. W. Heidbrink[4)]
[1)] National Institute for Fusion Science, 322-6 Oroshi-cho, Toki, Gifu 509-5292, Japan
[2)] General Atomics, P.O. Box 85608, San Diego, California 92186-5608, USA
[3)] Japan Atomic Energy Agency, 2-166 Omotedate, Obuchi, Rokkasho 039-3212, Japan
[4)] University of California, Irvine, California 92697, USA
E-mail contact of main author: todo@nifs.ac.jp

A multi-phase simulation that is a combination of classical simulation and hybrid simulation for energetic particles interacting with a magnetohydrodynamic (MHD) fluid is developed to simulate the nonlinear dynamics on the slowing down time scale of the energetic particles. The hybrid simulation code MEGA is extended with realistic beam deposition profile, collisions, and losses, and is used for both the classical and hybrid phases [1]. The multi-phase simulation is applied to DIII-D discharge #142111 where the fast ion spatial profile is significantly flattened due to multiple AE modes [2]. In the simulation, the stored fast ion energy is saturated due to AE modes at a level lower than in the classical simulation. After the stored fast ion energy is saturated, the hybrid simulation is run continuously. It is demonstrated that the fast ion spatial profile is flattened due to the interaction with the multiple AE modes with amplitude $v/v_A \sim \delta B/B \sim O(10^{-4})$. The fast ion pressure profile is close to that in the experiment. The dominant AE modes are toroidal Alfvén eigenmodes (TAE modes). The amplitude of the temperature fluctuations brought about by the TAE modes is of the order of 1% of the equilibrium temperature. These are consistent with electron cyclotron emission measurement in the experiment. Temperature fluctuations due to two of the toroidal Alfvén eigenmodes (TAE modes) are compared in more detail with the experimental measurement. The radial profiles and phases are in very good agreement with the measurement, and the amplitude is also in agreement within a factor of 2.

We have investigated nonlinear evolution of Alfvén eigenmodes and beam ions in DIII-D discharge #142111 at $t=525$ms. The equilibrium is reconstructed with the EFIT code, and a realistic beam ion deposition profile is given by the TRANSP code. Collisions (slowing down, pitch angle scattering, energy diffusion) with realistic physics parameters are taken into account. Particle losses are assumed to take place at the plasma boundary ($r/a=1$). 8 million particles are injected with a constant time interval in 150ms, although both the classical and multi-phase simulations are terminated before $t=150$ms. The beam injection power is 4.95MW with the full energy component. The half and third energy components are not included in this simulation. In the experiment, AE modes with toroidal mode number $n=1\text{-}5$ are observed at $t\sim525$ms [2]. Then, we restrict the energetic particle drive in the simulation to $n=1\text{-}5$ in order to reduce numerical noise. The numbers of grid points are (128, 128, 256) for $(R, \varphi, z)$ coordinates, respectively. Figure 1 shows the time evolution of stored fast ion energy. In the multi-phase simulation, the classical simulation was run for 4ms and alternately the hybrid simulation was run for 1ms. This set was repeated until stored fast ion energy is saturated at $t=75$ms. Beyond $t=75$ms, the hybrid simulation with MHD is continued, and the MHD fluctuation reaches to a steady level. Figure 2 compares the fast ion pressure profiles among the classical and multi-phase simulations, and the experiment. We see in Fig. 2 that the fast ion pressure profile in the multi-phase simulation is significantly flattened due to AE modes. At $t\geq75$ms, the beam injection is balanced with transport and energy loss due to collisions and the multiple AE modes.

We analyzed the bulk temperature fluctuation spectra with toroidal mode number $n=1\text{-}5$ at $r/a=0.4$ for $t \geq 75$ms. We found the temperature fluctuation normalized by the equilibrium temperature is $\delta T/T \sim O(10^{-2})$ that is comparable to the experiment. We have compared in detail the temperature fluctuation profile in the simulation with the ECE measurement for toroidal mode number $n=3$ and $4$. For the comparison with the electron temperature fluctuation in the experiment, we simply divide the MHD temperature fluctuation by a factor of 2. We found very good agreement in spatial profile, amplitude, and phase between simulation and experiment. Figure 3 compares temperature fluctuation profiles for $n=3$. We have agreement in amplitude within a factor of 2 for both $n=3$ and $n=4$. Figure 4 demonstrates excellent agreement in oscillation phase profile of temperature fluctuation for $n=3$. The interaction with energetic particles relaxes the restriction of ideal MHD model where oscillation phase is 0 or ±π because of the Hermitian property. The agreement in fast ion pressure profile and temperature fluctuation profiles validates the multi-phase simulation based on MHD model.

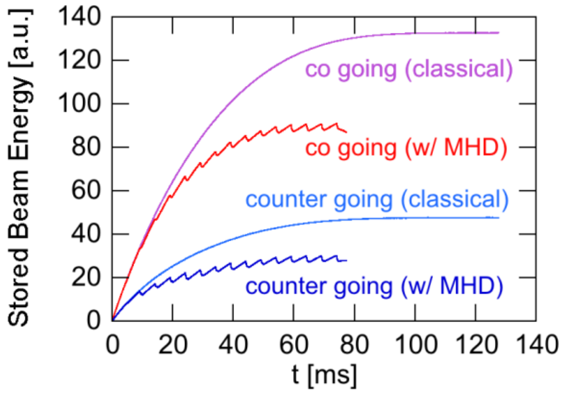

Fig. 1. Evolution of stored fast ion energy for classical and multi-phase simulations with MHD perturbations.

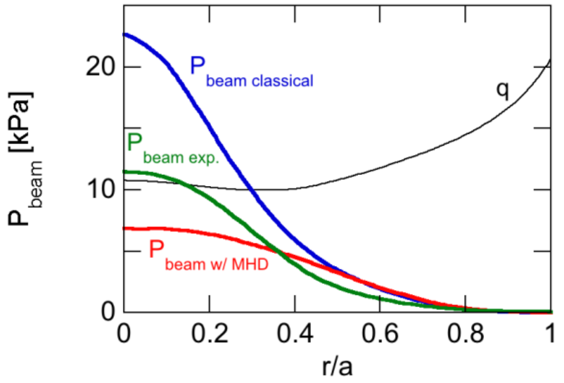

Fig. 2. Comparison of fast ion pressure profile among multi-phase simulation with MHD perturbations, classical simulation, and experiment.

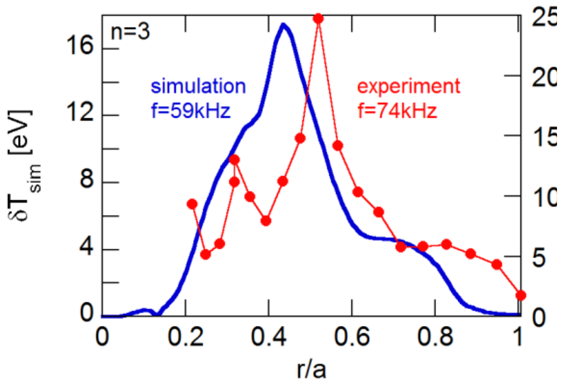

Fig. 3. Comparison of temperature fluctuation profile between simulation and experiment for $n=3$. The left vertical axis is for simulation, while the right for experiment.

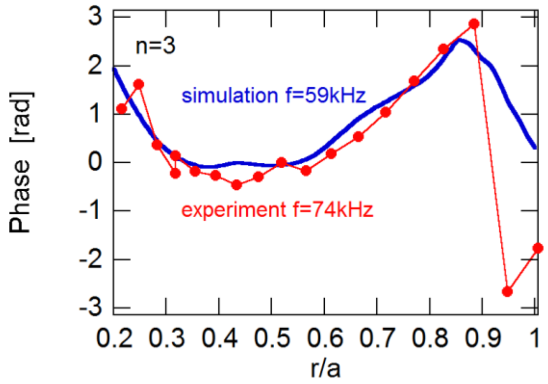

Fig. 4. Comparison of temperature fluctuation phase profile between simulation and experiment for $n=3$.

References
[1] Todo Y. *et al* submitted to *Nucl. Fusion*
[2] Van Zeeland M. A. *et al* 2012 *Nucl. Fusion* **52** 094023

# Scheme-independent error in entropy conservation in turbulent kinetic simulations

M. Lesur
*Itoh Research Center for Plasma Turbulence, Kyushu University*

Resonant interactions between particles and waves are relevant to a wide range of collisionless laboratory and space plasmas. Particle trapping in the troughs of electric potential is a fundamental kinetic nonlinearity, which leads to the formation of vortex-like structures in phase-space [1,2], especially in regimes of strong resonance. These structures have important impacts on wave stability, turbulent transport, intermittency, anomalous resistivity, heating, flows, etc. [3,4]

Accurate numerical simulation of such kinetic nonlinearities is challenging. Indeed, trapping involves the filamentation of phase-space (phase-space mixing). In the collisionless limit, numerical discretization replaces collisions to dissipate the smallest scales. A concern is that numerical dissipation and other simple models of collisions are artificial, and may impact the physics of interest. In this work, I show that the evolution of observables is surprisingly robust to changes of numerical treatment, which suggests that the details of small-scales dissipation are irrelevant. In particular, a systematic error of 15% in entropy conservation is found, regardless of the numerical treatment, without impacting observables.

In this work, as a paradigm for kinetic models in the presence of strong resonances, I restrict the analysis to one-dimensional ion-electron plasma with an initial velocity drift. The mass ratio is $\mathrm{m_i/m_e} = 4$, the ion and electron temperatures are equal, and the initial velocity drift is $\mathrm{v_d} = 4.2\mathrm{v_{T,i}}$ (slightly above linear instability threshold), where $\mathrm{v_{T,i}}$ is the ion thermal velocity. No collision operator is included. The simulation code is COBBLES [5], which is based on the Constrained-Interpolation-Profile, Conservative Semi-Lagrangian (CIP-CSL) scheme [6]. In this scheme, the evolutions of space- and velocity-integrals of the distribution function are computed from separate kinetic equations, along with the evolution of the distribution function itself. The implementation guaranties the local conservation of density. Fig.1 shows the redistribution of electrons and ions. Redistribution is due mainly to the evolution and interaction of phase-space structures (phase-space turbulence) [3].

Of common knowledge is that accurate simulations require careful treatment of conserved physical quantities, such as total mass, total energy and total entropy. For example, to obtain the turbulent steady-state accurately, spurious heating must be avoided. It is less

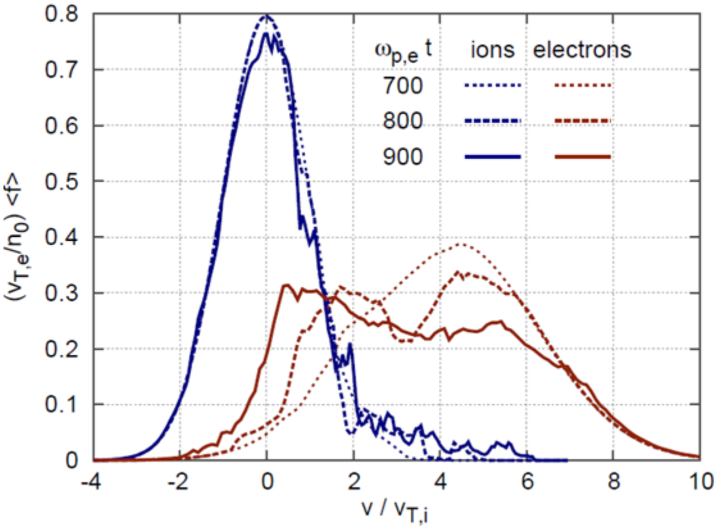

*Fig.1. Snapshots of the velocity distributions.*

known that the conservation properties strongly depend on the simulated physics. With the COBBLES code for two-species ion-acoustic turbulence, compared to one-species simulations of the dissipative bump-on-tail instability, the conservation of energy and entropy are degraded by several orders of magnitude. However, the quality of conservation is still satisfying, even in the long-time, fully nonlinear evolution of ion-acoustic turbulence. Indeed, the relative error in total energy remains below 0.1%.

Let me now focus on the entropy, which is trivially conserved in the physical model. The Fig.2 (a) shows the time-evolution of the error in electron entropy conservation, in COBBLES for four different numbers of grid points, and in a Particle-In-Cell (PIC) code, PICKLES, for two different numbers of particles. The error in total electron entropy conservation is well below 0.0001%, until phase-space filamentation occurs. Then, it quickly increases to 15%. Surprisingly, this error does not depend on the number of grid points, the number of particles, the time-step width (not shown in this figure), or even the type of numerical approach (Semi-Lagrangian or PIC). Although I don't have any clear explanation for this observation, one hypothesis is that the error in entropy conservation is actually a measure of infinitely small phase-space structures that are created during the nonlinear saturation.

A 15% error in entropy conservation is troubling. However, I didn't find any impact on the time-evolution of electric field, anomalous resistivity, or velocity distribution. As an example, Fig.2 (b) shows the time-evolution of electric field amplitude. In particular, let me compare two COBBLES simulations, with 256x1024 and 1024x1024 grid points. The time traces of electric field amplitude are almost perfectly overlapping, even though there is a significant discrepancy in the error in entropy conservation (14% and 15%).

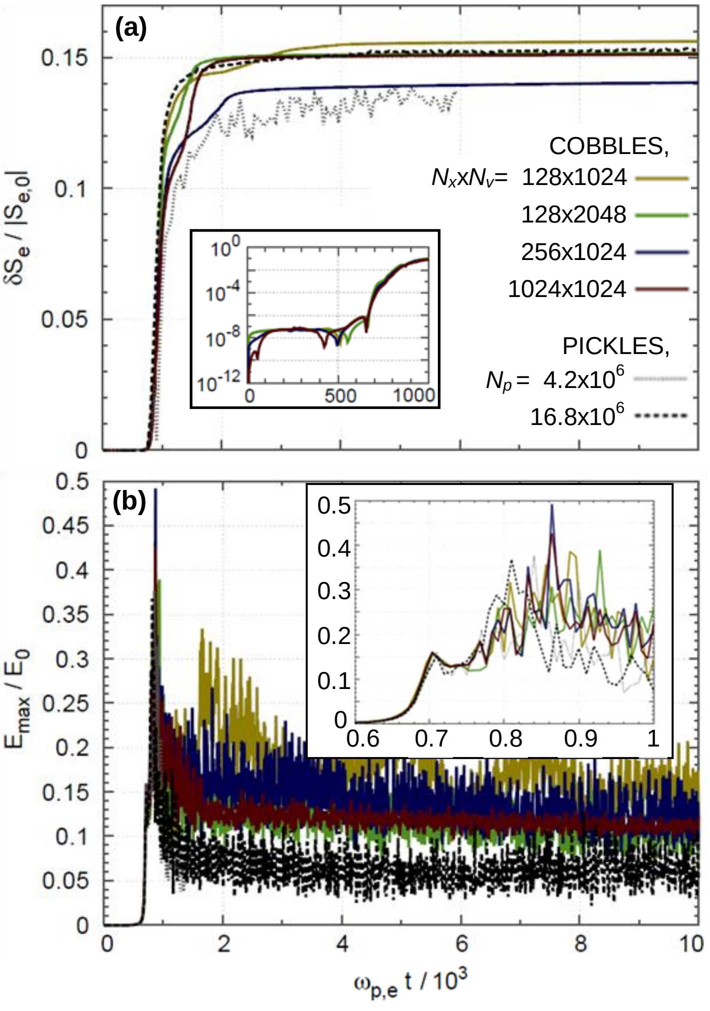

*Fig.2. Time evolution of (a) error in entropy conservation and (b) electric field amplitude. Insets: zoom on a smaller timescale. The legend is shared.*

[1] H. Schamel, Phys. Scr. **20**, 336 (1979)

[2] T.H. Dupree, Phys. Fluids **15**, 334 (1982)

[3] M. Lesur, submitted to Plasma Phys. Contr. Fusion

[4] Y. Kosuga et al., Nucl. Fusion **53**, 043008 (2013)

[5] M. Lesur, Y. Idomura, and X. Garbet, Phys. Plasmas **16**, 092305 (2009)

[6] T. Nakamura et al., J. Comput. Phys. **174**, 171 (2001)

# ITER Remote experimentation Centre

Takahisa Ozeki
Fusion Research and Development Directorate
Japan Atomic Energy Agency

Plan of ITER remote experimentation center (REC) based on the broader approach (BA) activity of the joint program of Japan and Europe (EU) is presented. Objectives of REC activity are 1) to identify the functions and solve the technical issues for the construction of the REC for ITER at Rokkasho, 2) to develop the remote experiment system and verify the functions required for the remote experiment by using the Satellite Tokamak (JT-60SA) facilities in order to make the future experiments of ITER and JT-60SA effectively, and 3) to test the functions of REC and demonstrate the total system by using JT-60SA and existing other facilities in EU. Preliminary identified items to be developed are 1) Functions of the remote experiment system, such as setting of experiment parameters, shot scheduling, real time data streaming, communication by video-conference between the remote-site and on-site, 2) Effective data transfer system that is capable of fast transfer of the huge amount of data between on-site and off-site and the network connecting the REC system, 3) Storage system that can store/access the huge amount of data, including database management, 4) Data analysis software for the data viewing of the diagnostic data on the storage system, 5) Numerical simulation for preparation and estimation of the shot performance and the analysis of the plasma shot. Detailed specifications of the above items will be discussed and the system will be made in these three years in collaboration with facilities of JT-60SA and EU tokamak, experts of informatics, activities of plasma simulation and ITER. Finally, the total system of REC will be demonstrated by the middle of 2017.

*Remote experiment system:* The concept of shot schedule of remote experiment and the required overall function are identified. The sequence of the procedure of the remote participation will be like that in Fig. 1. The right side of the figure is the main site of ITER in

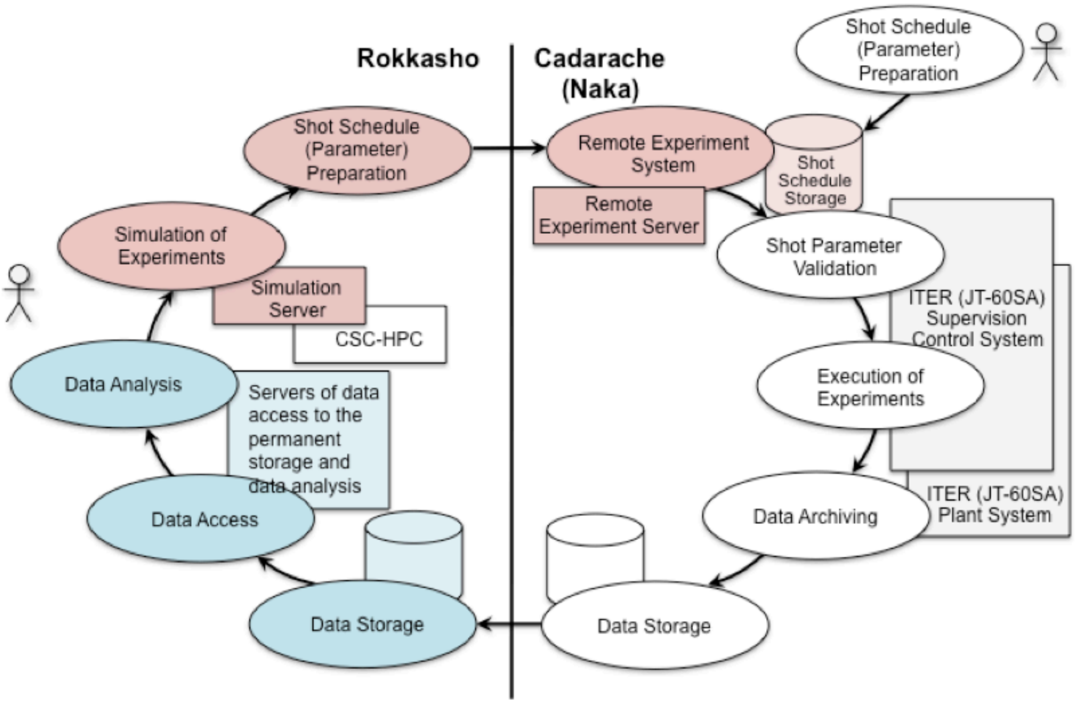

Fig.1. Concept of the shot schedule of the remote experiment

Cadarache (or JT-60SA in Naka), and the left side of the figure is a remote site (Rokkasho). Shot parameter prepared by the on-site researcher will be sent to the shot schedule storage, and the experiment will be executed by using this shot parameter after the validation check from the viewpoints of the safety and the operation of the facility. After the execution of experiment, the measured data are acquired and stored. Remote-site researcher will prepare the shot parameters in the same manner as the on-site researcher, and the shot schedule will be sent to the same shot schedule storage through a remote experiment server. To prepare the shot schedule, the remote-site researcher will first access the data storage of the remote site or the main site, analyze the previous shot data and then prepare the next shot parameters with the aid of simulations. On the remote site, it is important to perform fusion experiments under the same condition as the on-site researchers. Main functions to achieve this are preparation and setting of shot parameters, viewing the status of control data, streaming of the plasma status, data-exchange function of shot events, and monitoring of the facility operation. In addition, for the remote-site researchers, some tool that provides the atmosphere of being at the control room of the real facility is needed. Also, we need tools for smooth communication between the remotes and main sites.

*Fast data transfer and Storage:* In ITER, the amount of data to be experimentally measured can be expected to increase up to more than 1TB per discharge, and the amount of the accumulated data will be an order of 1PB in a year. Therefore, the fast data transfer and the large storage are critical issues in the remote site. For the network connection, broadband network system with larger than 10 Gbps is necessary for REC. The network in Rokkasho site has been connected to the nearest data center (Hirosaki data center) of SINET4 by 10 Gbps line in 2012 in collaboration with National Institute of Informatics (NII). Upgrade of the network bandwidth would be expected to more than 100 Gbps in future. To obtain the fast data transfer, investigations of effective data transfer method, development of accelerators, etc. are needed. For the data storage system, high reliability (redundancy), high accessibility (high-speed storage network), extendablity (scalability) and easy maintenance are required. However, for analysis and reference of experimental data from the remote site, it is not efficient to access data of the on-site storage each time. Therefore, the storage system on the remote site is necessary for efficient data analyses. Also, investigations of data storage method and data management in order to find the best way of data mining from the huge amount of data are also needed.

*Simulation and Data analysis:* In experiments of large facility such as ITER, the cost of per discharge is high, and the machine-time must be shared by many researchers. Therefore, in order to make effective use of the limited machine time, it is important to improve the environment for the shot preparation and the data analyses. This can be performed by detailed data analysis and more efficient plasma performance prediction by the simulation. For the data analysis software, analyses of experimental data should be done from the remote site using the on-site software and also the remote-site software. Functions of the data viewing of plasma diagnostics, statistical analyses of diagnostic data and mapping of diagnostic data are necessary. Front-end program to prepare the detailed and complicated data analysis and simulation codes, i.e. interface to the plasma analyses codes, such as the high energy particle phenomena, MHD stability, plasma turbulence, etc. will be needed. Numerical simulation is useful for the experiment. Simple simulation code of the plasma discharge, such as plasma current, plasma shape, etc. for the pulse preparation is needed as a first step. In order to evaluate a plasma performance, the integrated simulation including the plasma model of the transport, MHD, divertor, etc. will be needed in the next step. To realize the simulation, it is necessary to collaborate with the activities of the integrated code, etc.